Dynactin interaction with AP-2 adaptor complex requires CLIP-170 and autophagy

Aleksandra Tempes,[1, *] Karolina Bogusz,[1, *] Agnieszka Brzozowska,[1, *] Jan Weslawski,[1] Matylda Macias,[1, 2] Aleksandra Lew,[1] Malgorzata Calka-Kresa,[3] Tytus Bernas,[3,4] Andrzej A. Szczepankiewicz,[3] Magdalena Bakun,[5] Tymon Rubel,[6] Anna R. Malik,[1, 7, $] and Jacek Jaworski[1, $]

[1] Laboratory of Molecular and Cellular Neurobiology, International Institute of Molecular and Cell Biology, Warsaw, Poland

[2] Microscopy and Flow Cytometry Core Facility, International Institute of Molecular and Cell Biology, Warsaw, Poland

[3] Nencki Institute of Experimental Biology, Polish Academy of Sciences, Warsaw, Poland

[4] Microscopy Facility, Department of Anatomy and Neurology, Virginia Commonwealth University School of Medicine, Richmond, VA, USA

[5] Institute of Biochemistry and Biophysics, Polish Academy of Sciences, Warsaw, Poland

[6] Institute of Radioelectronics and Multimedia Technology, Warsaw University of Technology, Warsaw Poland

[7] Faculty of Biology, University of Warsaw, Warsaw, Poland

* Equal contribution

[$] Corresponding authors: **Jacek Jaworski**, ORCID ID: 0000-0001-8760-7865
Laboratory of Molecular and Cellular Neurobiology
International Institute of Molecular and Cell Biology
Ks. Trojdena St. 4, Warsaw, 02-109, Poland
Phone: +48 22 597 07 55
Email: jaworski@iimcb.gov.pl

Anna R. Malik, ORCID ID: 0000-0001-7732-0756
Cellular Neurobiology Research Group
Institute of Developmental Biology and Biomedical Sciences,

Faculty of Biology, University of Warsaw
Miecznikowa St. 1, Warsaw, 02-096, Poland
Phone +48 22 554 10 19
Email: ar.malik@uw.edu.pl

Abstract

The endocytic adaptor protein 2 (AP-2) complex binds dynactin as part of its noncanonical function, which is necessary for dynein-driven autophagosome transport along microtubules in neuronal axons. The absence of this AP-2-dependent transport causes neuronal morphology simplification and neurodegeneration. The mechanisms that lead to formation of the AP-2–dynactin complex have not been studied to date. However, inhibition of the mammalian/mechanistic target of rapamycin complex 1 (mTORC1) enhances the transport of newly formed autophagosomes, by influencing the biogenesis and protein interactions of Rab-interacting lysosomal protein (RILP), another dynein cargo adaptor. We tested the effects of mTORC1 inhibition on interactions between the AP-2 and dynactin complexes, with a focus on their two essential subunits, AP-2β and $p150^{Glued}$. We found that the mTORC1 inhibitor rapamycin enhanced AP-2–dynactin complex formation in both neurons and non-neuronal cells. The live imaging of neuronal axons revealed that when combined with brain-derived neurotrophic factor (BDNF), an agonist of tropomyosin receptor kinase B (TrkB), rapamycin also increased the number of retrogradely moving mobile AP-2β-$p150^{Glued}$ complexes. Additional analysis revealed that the AP-2β–$p150^{Glued}$ interaction was indirect and required integrity of the dynactin complex. Rapamycin-driven enhancement of the AP-2–dynactin interaction also required the presence of cytoplasmic linker protein 170 (CLIP-170) and activation of autophagy. The latter was sufficient to enhance the AP-2β interaction with $p150^{Glued}$, even when mTORC1 was active. Altogether, our results show that autophagy regulates the AP-2–dynactin interaction to coordinate sufficient motor-adaptor availability for newly generated autophagosomes.

Keywords: dynactin, $p150^{Glued}$, AP-2 adaptor complex, mTORC1, CLIP-170, autophagy

Abbreviations: ANOVA - analysis of variance; ALR - autophagic lysosome reformation; Arp-1 - actin-related protein 1; AP2 – adaptor complex 2; AP-2β: AP-2 complex subunit beta; BDNF - brain-derived neurotrophic factor; CC1 - coiled-coil 1; CC2 - coiled-coil 2; CLIP-115 - cytoplasmic linker protein 115; CLIP-170 - cytoplasmic linker protein 170; DMEM - Dulbecco's modified Eagle's medium; EB3 – end binding protein 3; EGFP – enhanced green fluorescent protein; EM-PLA – electron microscopy proximity ligation assay; GST - Glutathione S-transferase; IP – immunoprecipitation; LC3 - microtubule-associated protein 1A/1B-light chain 3; mTORC1 - Mammalian/mechanistic target of rapamycin complex 1; PBS – phosphate buffered saline; $p150^{Glued}$ – dynactin subunit 1; PLA – proximity ligation assay; RILP - Rab-interacting lysosomal protein; +TIP – plus end tracking protein; TrkB - tropomyosin receptor kinase B

Introduction

The effective cooperation of endomembrane components and the cytoskeleton is necessary for efficient intracellular communication and cell contacts with the extracellular environment. Microtubules are cytoskeleton elements that are essential for both the integrity of membrane compartments and their long-distance movement [1, 2]. Microtubules are dynamic and polarized, meaning that their ends (referred to as plus and minus) can undergo dynamic changes and are not identical [3]. This polarization determines the rules of directed cargo transport along microtubules by molecular motors (e.g., kinesins and dynein; Hirokawa et al., 2009; Schroer, 2004). The latter transports cellular cargo from the plus end to the minus end of microtubules [5–7]. In non-polarized cells and neuronal axons, this means transport from the cell periphery toward the nucleus (i.e., retrograde transport). Dynein does not act alone; it requires additional protein complexes to efficiently hold cargo and move along microtubules. One of these complexes is dynactin, a large multiprotein complex that initiates dynein movement, increases its processivity, and supports cargo attachment [5, 8, 9]. Dynactin consists of two major parts: sidearm and actin-related protein 1 (Arp-1) rod [5, 7, 10, 11]. The sidearm consists of $p150^{Glued}$, p50, and p24 [5, 7, 10, 11]. The Arp-1 rod is further divided into Arp-1-polymer, pointed-end complex (Arp11, p62, p27, p25), and CapZ a/b, which cooperatively with dynein activators and adaptors is responsible for cargo binding [5, 7, 10–15]. $p150^{Glued}$ is the largest dynactin subunit, containing four domains. Most of the N-terminal region with a Cap-Gly domain binds microtubules and other microtubule-binding proteins that specifically recognize microtubule plus ends. It is followed by coiled-coil 1 (CC1; which is known to bind dynein), coiled-coil 2 (CC2), and the C-region [16]. The C-region of $p150^{Glued}$, together with p50 and p24, forms a sidearm shoulder that is responsible for tethering both parts of dynactin [16].

Cytoplasmic linker protein 170 (CLIP-170) was the first identified member of the microtubule plus-end tracking protein (+TIP) family [17–19]. It interacts with $p150^{Glued}$, which also belongs to this family [20]. The binding of $p150^{Glued}$ to microtubule plus ends and its plus-end tracking behavior require the presence of CLIP-170 [21, 22]. In some model systems (e.g., neuronal axons), this is essential for the initiation of dynein-dynactin-bound cargo transport along tyrosinated microtubules [8, 23]. However, the best-studied function of CLIP-170 is different and concerns its function that promotes microtubule plus-end growth [24]. CLIP-170 may also bridge microtubules with the actin cytoskeleton [25, 26].

The adaptor protein 2 (AP-2) complex consists of two large subunits (α, β), one medium subunit (μ), and one small subunit (σ; Collins et al., 2002). All four subunits contribute to the trunk of the AP-2 complex, but α and β2 C-termini project outside the trunk as α and β2 appendages (i.e., ears), respectively [27]. Canonically, AP-2 serves as a cargo adaptor complex in clathrin-mediated endocytosis (Traub, 2003). However, evidence supports AP-2 functions outside the initiation of clathrin-mediated endocytosis, particularly in macroautophagy (hereafter called autophagy; [29–34].

Autophagy is a cellular process during which cells trap proteins or organelles (e.g., mitochondria) that are designated for degradation in double-membrane structures, called autophagosomes, and deliver them to lysosomes [35–38]. Autophagosome formation is a multistep process. Mammalian/mechanistic target of rapamycin complex 1 (mTORC1) is among its best-known regulators [39, 40]. The best understood is how low mTORC1 activity allows autophagy initiation, but autophagosome maturation, microtubular transport, and fusion with the lysosome also require mTORC1 inhibition [41–46].

Autophagosomes are transported along microtubules. Dynein-dynactin transports autophagosomes retrogradely for fusion with lysosomes [47–49]. The ways in which autophagosomes attach to dynein-dynactin are still debated, even in the case of neurons in

which this aspect has been the most extensively studied. For example, some reports suggest that autophagosomes in neurons are transported by dynein only after fusion with late endosomes that already carry dynein-dynactin [29, 31, 50, 51], whereas others show that autophagosomes are transported alone and fuse with late endosomes and lysosomes on their way toward the cell soma [2, 45, 47, 52, 53]. Although these discrepancies are not yet resolved, neuronal amphisomes that are produced by autophagosome-late endosome fusion are not merely carriers of used or unwanted presynaptic content for degradation. They also act as signaling organelles that carry activated receptors for neurotrophins, such as tropomyosin receptor kinase B (TrkB; Andres-Alonso et al., 2019; Kononenko et al., 2017) to the cell soma. AP-2 was recently shown to act as an adaptor for the retrograde transport of amphisomes. The lack of this AP-2-dependent transport in axons resulted in disturbances in the morphology of dendrites and neurodegeneration [29, 31]. For dynein cargo adaptor function, AP-2 binds microtubule-associated protein 1A/1B-light chain 3 (LC3) on the amphisome surface via its AP-2μ subunit, whereas the AP-2β ear was shown to co-immunoprecipitate with $p150^{Glued}$ [31].

Although AP-2–dynactin was shown to transport TrkB-positive amphisomes, further details of the AP-2–dynactin interaction and its potential regulation are missing. The latter is particularly intriguing when considering findings that different kinases regulate LC3-adaptor binding and/or the axonal transport of autophagosomes [45, 52]. A recent study showed that dynein can be recruited to autophagosomes by LC3 and Rab-interacting lysosomal protein (RILP) when mTORC1 activity is low [45]. These findings raise the question of whether the AP-2–$p150^{Glued}$ interaction and transport are regulated by mTOR activity. If so, then what is the mechanism of the mTORC1 contribution? Here, we found that mTORC1 inhibition enhanced the AP-2–$p150^{Glued}$ interaction in both neurons and non-neuronal cells. In neurons, when combined with the TrkB agonist brain-derived neurotrophic factor (BDNF), rapamycin treatment increased the number of retrogradely moving AP-2–$p150^{Glued}$ complexes in axons.

We also found that AP-2–p150^{Glued} complex formation, boosted by mTORC1 inhibition, in non-neuronal cells required an intact dynactin complex, the presence of CLIP-170, and the initiation of autophagy. Additionally, we found that autophagy induction, even in the presence of mTORC1 activity, was sufficient to enhance formation of the AP-2–dynactin complex. Thus, we reveal a novel mechanism whereby the functions of essential components of cellular transport machinery are regulated at the level of autophagy initiation. This mechanism may be key to ensuring coordinated actions of all elements of this complex system that are vital for basic cellular functions.

Materials and Methods

Plasmids and siRNA

The following plasmids were commercially available or described previously: pEGFPC1 (Clontech), β-actin-GFP and β-actin-tdTomato [83], HA-BirA [84], pAvi-tag-thrombin-HA (also known as Bio-Thrombin-HA; [85], pEGFPC1-Ap2b1 [86], pEGFPC2-Avi-tag-p150^{Glued} [31], pEGFPC2-Avi-tag-βGal (also known as bioβ-Gal; Swiech et al., 2011), EB3-GFP [60], pEGFP-CLIP-170 and pEGFPC1-CLIP-170-Δhead (Komarova et al., 2002; gift from Anna Akhmanova), pEGFPC1-p50 (Hoogenraad et al., 2001; gift from Casper Hoogenraad), pET-28-His$_6$-AP-2β appendage domain [31], pGEX-4T1 (Merck, catalog no. GE28-9545-49), and pGEX-4T1-GST-Eps15 (aa 541-790; gift from Mark McNiven; [56]. β-actin-GFP-p150^{Glued} and β-actin-tdTomato-p150^{Glued} were obtained by polymerase chain reaction (PCR)-based subcloning of the p150^{Glued} coding sequence into SalI/NotI sites of β-actin-GFP and β-actin-tdTomato, respectively. pAvi-tag-thrombin-HA-p150^{Glued}N plasmid that encoded a fragment of p150^{Glued} (aa 1-490) was obtained by PCR using the following primers: 5'-GAAGAATTCATGGCCCAGAGCAAGAGGAC-3' and 5'-GCGGGCGGCCGCTTAGGCGGCTTCCACTCGCTTCTG-3', with pEGFPC2-Avi-tag-

p150^{Glued} as a template. The resulting product was inserted into EcoRI/NotI restriction sites of pAvi-tag-thrombin-HA. pAvi-tag-thrombin-HA-p150^{Glued}C plasmid that encoded a fragment of p150^{Glued} (aa 490-1278) was generated analogically using the following primers: 5'-GAAGAATTCATGGCAGGCGCCCGAGTAAGG-3' and 5'-GCGGGCGGCCGCTTAGGAGATGAGACGACCGTGAAG-3'. The pAvi-tag-thrombin-HA-p150^{Glued}C2 plasmid that encoded a fragment of p150^{Glued} (aa 1049-1278) was generated using 5'-GAAGAATTCATGGGCACTCCTGGGCAGGCTCCAGGCGC-3' and 5'-GCGGGCGGCCGCTTAGGAGATGAGACGACCGTGAAG-3' primers, with pAvi-tag-thrombin-HA-p150^{Glued}C as a template. The resulting product was inserted into EcoRI/NotI restriction sites of pAvi-tag-thrombin-HA. The GST-p150^{Glued}C plasmid that encoded a fragment of p150^{Glued} (aa 490-1278) with a GST tag was generated by PCR from the HA-Avi-tag-p150^{Glued}C plasmid using 5'-GAAGAATTCATGGCAGGCGCCCGAGTAAGG-3' and 5'-GCGGGCGGCCGCTTAGGAGATGAGACGACCGTGAAG-3' primers. The product was inserted in pGEX-4T1 into EcoRI/NotI restriction sites. The GST-p150^{Glued}C2 plasmid that encoded a fragment of p150^{Glued} (aa 1049-1278) with a GST tag was obtained by PCR analogically using 5'-GAAGAATTCATGGGCACTCCTGGGCAGGCTCCAGGCGC-3' and 5'-GCGGGCGGCCGCTTAGGAGATGAGACGACCGTGAAG-3' primers. The following siRNAs were purchased from Invitrogen: Select Negative Control No. 1 siRNA (catalog no. 4390843; siCtrl), Silencer Select siRNA rat Clip1 #1 (catalog no. 4390771, ID: s134775; siCLIP-70), and Silencer Select siRNA human Clip1 #1 (catalog no. 4392420, ID: s12372; siCLIP-170).

Antibodies

Commercially available primary antibodies that were used for this study are listed in Table 1. Rabbit anti-pan CLIP antibody (clone 2221; Western blot, 1:500) that recognized both

CLIP-115 and CLIP-170 was a gift from Casper Hoogenraad [88]. Alexa Fluor 488-, 568-, 594-, and 647-conjugated secondary antibodies (anti-mouse, anti-goat, and anti-rabbit) were obtained from Thermo Fisher. Horseradish peroxidase (HRP)-conjugated secondary antibodies were obtained from Jackson ImmunoResearch. Anti-mouse/anti-rabbit IRDye 680RD and IRDye 800CW were purchased from LI-COR Biosciences.

Table 1. Primary antibodies used for the study.

Primary antibody	Manufacturer, catalog no.	Application, dilution
mouse anti-p150^{Glued}	BD Bioscience, BD610474	PLA 1:100 WB 1:1000 IF 1:200 IP 2 μg/reaction
rabbit anti-p150^{Glued}	Cell Signaling Technology, 69399	WB 1:1000
rabbit anti-AP-2β	Thermo Fisher, PA1-1066	PLA 1:100 IP 2 μg/reaction IF 1:250
rabbit anti-AP-2β	Santa Cruz Biotechnology, sc-10762	WB 1:500
mouse anti-AP-2β	Santa Cruz Biotechnology, sc-74423	WB 1:500
goat anti-AP-2β	Santa Cruz Biotechnology, sc-6425	IF 1:200 IP 10 μg/reaction
mouse anti-Arp1	Santa Cruz Biotechnology, sc-376010	WB 1:250
mouse anti-p62	Santa Cruz Biotechnology, sc-55603	WB 1:250
mouse anti-DIC1/2	Santa Cruz Biotechnology, sc-13524	WB 1:250
Rabbit anti-phospho-S6 Ser235/236	Cell Signaling Technology, 4858	WB 1:1000 IF 1:200
mouse anti-S6	Cell Signaling Technology, 2217	WB 1:1000
mouse anti-CLIP-170	Santa Cruz Biotechnology, 28325	WB 1:500 IF 1:500
rabbit anti-GFP	MBP, 598	WB 1:1000
mouse anti-tubulin	Sigma-Aldrich, T5168	WB 1:5000 IF 1:500
rabbit anti-tubulin	Abcam, ab4074	WB 1:3000
rabbit anti-LC3B	Sigma-Aldrich, L7543	WB 1:2500 IF 1:200
mouse anti-beclin-1/BECN1	Santa Cruz Biotechnology, sc-48341	WB 1:250
rabbit anti-phospho-beclin-1 Ser30	Cell Signaling Technology, 54101	WB 1:500
mouse anti-actin	Sigma-Aldrich, A4700	WB 1:1000
rabbit anti-IgG	Cell Signaling Technology, 3900	IP 2 μg/reaction
goat anti-IgG	Sigma-Aldrich, I5256-10MG	IP 10 μg/reaction
rabbit anti-neurofascin	Antibodies Incorporated, 75-172	Live imaging 1:100
mouse anti-his-tag	Cell Signaling Technology, 2366	WB 1:1000
rat anti-GST-tag	Chromotek, 6g9-100	WB 1:1000
rabbit anti-HA-tag	Cell Signaling Technology, 3724	WB 1:1000

PLA, proximity ligation assay; WB, Western blot; IF, immunofluorescence; IP, immunoprecipitation.

Cell line cultures and transfection

Rat2 and HEK293T cells were purchased from ATCC and grown in Dulbecco's

modified Eagle's medium (DMEM) that contained 10% fetal bovine serum (FBS) and 1% penicillin-streptomycin (all from Sigma-Aldrich) at 37°C in a 5% CO_2 atmosphere. For PLA and PLA-EM experiments, Rat2 cells were grown on glass coverslips or Thermanox plastic coverslips (Thermo Fisher; catalog no. 174950), respectively, coated with 0.2% gelatin for 1 h at 37°C. For live experiments, Rat2 cells were seeded on glass coverslips that were coated with poly-L-lysine (50 μg/ml in H_2O for 1 h). For plasmid DNA transfection, HEK293T cells at 70% confluency were transfected usi ng polyethylenimine PEI 25K (Polysciences, catalog no. 23966) according to the manufacturer's protocols. After transfection, HEK293T cells were grown in DMEM supplemented with 5% FBS for 48 h. Rat2 cells were transfected with plasmid DNA using electroporation. For each transfection, a total of 10^6 cells were suspended in Opti-MEM medium (Thermo Fisher, catalog no. 31985-047), mixed with 10 μg of DNA, and added to 2 mm gap cuvettes (Nepagene, catalog no. EC-002S). Cells were electroporated using a CUY21 electroporator (Nepagene) with poring pulses (6×, 150 V, 2.5 ms length, 50 ms interval, 10% decay rate), followed by transfer pulses (5×, 20 V, 50 ms length, 50 ms interval, five pulses, 40% decay rate) with "±" polarity set for both. After electroporation, the cells were grown in DMEM with 10% FBS without antibiotics. The medium was changed the next day for one that contained 1% penicillin-streptomycin. The siRNA transfection of HEK293T and Rat2 cells was performed on trypsinized cells using Lipofectamine RNAiMAX Transfection Reagent (Thermo Fisher, catalog no. LMRNA015) according to the manufacturer's protocol.

Primary neuron preparation and transfection

Primary hippocampal cultures were prepared from embryonic day 18 rat brains as previously described [26]. The rats that were used to obtain neurons for further experiments were sacrificed according to protocols that complied with European Community Council Directive 2010/63/EU. The transfections of hippocampal neurons were performed on DIV5

with Lipofectamine2000 (Thermo Fisher, catalog no. 11668019) as described previously [26], except that the incubation time with the transfection mixture was reduced to 2 h. DNA (2 µg) and 1.5 µl of Lipofectamine2000 were used per well of a 12-well dish.

Drugs and drug treatment

All drugs were dissolved in DMSO, the final concentrations of which in the culture medium did not exceed 0.1%. For mTOR inhibition, Rat2 and HEK293T cells were treated with rapamycin (100 nM, Calbiochem, catalog no. 553210) or AZD-8055 (100 nM, Cayman Chemical, catalog no. 16978-5) for 2 h before the experiment (see figure legends for detailed descriptions). For autophagy inhibition, 25 µM SBI-0206965 (Merck, catalog no. SML1540) was used for 2.5 h (see figure legends for detailed descriptions). When combined with rapamycin, SBI-0206965 was added 30 min before the addition of rapamycin. To induce autophagy independently from mTORC1 inhibition, 100 µM L-690330 (Tocris, catalog no. 0681) was added to cells for 3 h. Nocodazole (100 nM; Sigma-Aldrich, catalog no. M1404) was used to inhibit microtubule dynamics. For live cell imaging experiments, the drug was added to Rat2 cells 1 h before imaging. For PLA experiments, in which nocodazole was added to Rat2 cells alone or combined with rapamycin, it was added either 2 h 15 min or 1 h before fixation, depending on whether it was used before or after rapamycin treatment. Before live imaging or fixation, neurons were treated with either vehicle (0.1% DMSO, 2 h) or rapamycin (100 nM, 2 h). In selected variants, BDNF (50 ng/ml, Sigma-Aldrich, catalog no. SRP3014-10UG) was added additionally to vehicle- or rapamycin-pretreated cells 15 min before imaging or fixation.

Animals and rapamycin treatment

Rapamycin treatment and brain protein lysate isolation were performed according to a

protocol that was approved by the 1st Ethical Committee in Warsaw (Poland; decision no. 843/2008 and 288/2012). Mature (3-month-old) male Wistar rat were used for the experiments. Rapamycin was initially dissolved in 100% ethanol at a 0.1 mg/ml concentration and stored at -20°C. Immediately before the injection, rapamycin was diluted in a vehicle solution that contained 5% Tween 80 and 5% PEG 400 (low-molecular-weight grade of polyethylene glycol; Sigma) and injected intraperitoneally (i.p.; 10 mg/kg) three times per week for 1 week. A control group of rats was injected with a vehicle solution that contained 5% Tween 80, 5% PEG 400, and 4% ethanol. Protein extraction from adult rat brains was performed as described previously (Kononenko et al., 2017) with a slight modification that involved the addition of 100 nM rapamycin to the lysis buffer for brains of rapamycin-treated animals.

Proximity ligation assay

For the proximity ligation assay (PLA), cells were fixed for 5 min with ice-cold 100% methanol and 2 mM ethylene glycol-bis(β-aminoethyl ether)-*N*,*N*,*N'*,*N'*-tetraacetic acid (EGTA) at -20°C followed by 10 min with 4% paraformaldehyde (PFA)/ 4% sucrose in phosphate-buffered (pH 7.4). Fixed cells were washed three times with phosphate-buffered saline (PBS) and incubated with mouse anti-p150^{Glued} and rabbit anti-AP-2β antibodies diluted in PBS that contained 1% donkey serum and 0.2% Triton-X100 at 4°C overnight. The next day, the cells were washed twice for 5 min with PBS with 1% donkey serum and 0.2% Triton-X100, washed once for 1 min in antibody diluent that was provided in the manufacturer's PLA kit (Sigma-Aldrich, catalog no. DUO92101), and then incubated for 60 min at 37°C with relevant secondary antibodies conjugated to oligonucleotide PLUS or MINUS (Sigma-Aldrich; catalog no. DUO92002 and DUO92004, respectively) diluted in antibody diluent. The coverslips were then washed twice for 5 min with buffer A (Sigma-Aldrich, catalog no. DUO82046). Ligation and amplification were performed according to the manufacturer's

protocol using Duolink In Situ Detection Reagents Red (Sigma-Aldrich, catalog no. DUO92008). The cells were then counterstained with mouse anti-tubulin antibody diluted in PBS that contained 1% donkey serum and 0.2% Triton-X100 for 30 min at room temperature and washed three times with PBS and incubated with anti-mouse Alexa-488-conjugated secondary antibody diluted in PBS that contained 1% donkey serum and 0.2% Triton-X100 for 30 min at room temperature to visualize cell shape. Finally, the cells were washed three times with PBS and mounted with DuoLink *in situ* mounting medium that contained DAPI (Sigma-Aldrich, catalog no. DUO82040). For each experiment, negative controls that lacked one of the primary antibodies were used.

PLA-EM

For PLA-EM, Rat2 cells were grown for 24 h and fixed for 15 min in 4% PFA with the addition of 0.1% glutaraldehyde in PBS. The cells were then washed three times with PBS. Afterward, cells in PBS were permeabilized by three cycles of freezing in liquid nitrogen, thawed, incubated for 20 min with 1% sodium borohydride in PBS, washed three times with PBS, incubated for 20 min at room temperature with 3% hydrogen peroxide in PBS/ethanol (1:1), and washed again three times in PBS. Next, fixed and permeabilized cells were incubated for 1 h in 5% BSA in PBS at room temperature. Afterward, the cells were incubated for 48 h at 4°C with primary mouse anti-p150^{Glued} and rabbit anti-AP-2β antibodies diluted in 0.1% donkey serum/PBS and washed three times in PBS at room temperature. The cells were then incubated for 60 min at 37°C with PLA probes (Sigma-Aldrich, catalog no. DUO92002 and DUO92004) and washed twice for 5 min with buffer A (Sigma-Aldrich, catalog no. DUO82046). Ligation and amplification were performed according to the manufacturer's protocol using Duolink In Situ Detection Reagents Brightfield (Sigma-Aldrich, catalog no. DUO92012). After the PLA reaction, the cells were additionally fixed with 2.5%

glutaraldehyde in PBS for 2 h at 4°C and washed twice with PBS and once with deionized water. Next, the cells were incubated with 3% hexamethylenetetramine, 5% silver nitrate, and 2.5% disodium tetraborate for 10 min at 60°C, washed three times with water, once with 0.05% tetrachloroauric acid, once with 2.5% sodium thiosulfate, and finally three times with water (all at room temperature). As the last step, the cells were postfixed with 1% osmium tetroxide for 1 h at room temperature, washed with water, incubated in 1% aqueous uranyl acetate for 1 h, dehydrated with increasing dilutions of ethanol, and infiltrated with epoxy resin (Sigma-Aldrich, catalog no. 45-359-1EA-F). After resin polymerization in 60°C, fragments of coverslips with embedded cells were cut out with scissors and glued to the resin blocks. The blocks were then trimmed and cut with a Leica ultramicrotome (Ultracut R) to obtain ultrathin sections (70 nm thick) and collected on 100 mesh copper grids (Agar Scientific, catalog no. AGS138-1). Specimen grids were examined with a Tecnai T12 BioTwin transmission electron microscope (FEI) equipped with a 16 megapixel TemCam-F416 (R) camera (Tietz Video and Imaging Processing Systems).

Immunofluorescence

For analyses of the colocalization of $p150^{Glued}$ and AP-2β proteins, Rat2 cells were fixed with ice-cold 100% methanol with 2 mM EGTA for 5 min at -20°C and then with 4% paraformaldehyde (PFA)/ 4% sucrose in phosphate-buffered (pH 7.4) for 10 min at room temperature and washed three times with PBS. After fixation, the cells were blocked for 1 h in blocking buffer (5% donkey serum, 0.3% Triton X-1001 in PBS). Next, the cells were incubated overnight with primary antibodies in antibody dilution buffer (1% bovine serum albumin [BSA], 0.3% Triton X-100 in PBS) at 4°C and then washed three times with PBS at room temperature. Afterward, specimens were incubated with Alexa 488- and Alexa 594-conjugated secondary antibodies for 1 h at room temperature, followed by three washes with

PBS. Coverslips were mounted with Prolong Gold with DAPI (Thermo Fisher, catalog no. P36941). For the immunofluorescent staining of P-S6, neurons were fixed with 4% PFA/ 4% paraformaldehyde (PFA)/ 4% sucrose in phosphate-buffered (pH 7.4) for 10 min at room temperature and washed three times with PBS. After fixation, the cells were blocked for 1 h in blocking buffer (5% donkey serum, 0.3% Triton X-1001 in PBS). Next, the cells were incubated overnight with primary antibody in antibody dilution buffer I (1% BSA, 0.3% Triton X-100 in PBS) at 4°C and then washed three times with PBS at room temperature. Alexa 488-conjugated secondary antibody with Alexa 568-conjugated phalloidin in antibody dilution buffer were next added for 1 h at room temperature. Afterward, the cells were washed three times with PBS, and coverslips were mounted with Prolong Gold (Thermo Fisher, catalog no. P36934). For the immunofluorescent detection of CLIP-170, the cells were fixed for 5 min with ice-cold 100% methanol with 2 mM EGTA at -20°C, followed by 10 min with 4% paraformaldehyde (PFA)/ 4% sucrose in phosphate-buffered (pH 7.4) at room temperature, and then washed three times with PBS. Next, the cells were washed twice with antibody dilution buffer II (1% donkey serum, 0.2% Triton X-100 in PBS) and incubated overnight with the primary antibody in antibody dilution buffer II at 4°C. After incubation with primary antibodies, the cells were washed three times with PBS at room temperature and incubated with Alexa 488-conjugated secondary antibody in antibody dilution buffer II for 1 h at room temperature. Afterward, the cells were washed three times with PBS, and nuclei were stained with Hoechst 33258 (1 μg/ml; Thermo Fisher Scientific) for 5 min. The cells were then washed two more times with PBS, and coverslips were mounted with Prolong Gold. To analyze LC3B immunofluorescence, the cells were fixed according to the CLIP-170 staining protocol. After fixation, the cells were blocked for 15 min at room temperature in antibody dilution buffer III (2% donkey serum, 0.2% Triton X-100 in PBS) and incubated for 1 h with the primary antibody in antibody dilution buffer III at room temperature. The cells were then washed three times

with antibody dilution buffer III at room temperature and incubated with Alexa 488-conjugated secondary antibody in antibody dilution buffer III for 1 h at room temperature. The next steps were identical to the description of CLIP-170 immunofluorescence.

Fixed cell image acquisition and analysis

Microscopic images of fluorescently labeled *in vitro* cultured cells, with the exception of quantitative colocalization experiments, were acquired using a Zeiss LSM800 confocal microscope (40× or 63× oil objective) as Z-stacks at 0.2-0.5 μm intervals at 1024 × 1024 pixel resolution. To enable comparisons between images, the microscope settings were kept constant for all scans. The Z-stacks were converted to single images using a maximum intensity projection. For quantification of the number of PLA puncta in Rat2 cells, the cell shape was indicated as a region of interest for each cell, and the threshold was set manually and uniformly for all images in each experiment to extract specific signals from background. The number of PLA puncta per cell was counted in ImageJ software using the "Analyze Particles" macro. The average number of PLA puncta per cell was then calculated for each condition, and the results were normalized by subtracting the average number of PLA puncta per cell from the negative control. The obtained average number of PLA puncta per cell was further normalized by dividing the obtained values from a particular experiment by the average number of PLA puncta per cell from the control from at least three repetitions. For the analysis of P-S6 levels in neurons, the mean fluorescent intensity of P-S6 was measured in the neuronal soma using ImageJ software.

For quantitative colocalization analysis, images of fluorescently labelled cells were registered using Leica SP8 confocal microscope with 63x oil immersion Plan Apo objective lens (NA=1.4). The microscope system was equipped with acousto-optical beam splitter (AOBS) and multialkali single-channel PMTs and hybrid detectors (HyD). Fluorescence of

DAPI was excited with 405 nm light (5 mW diode laser) and detected in 410 – 470 nm range. Fluorescence of Alexa 488 and Alexa 568 was excited with supercontinuum (white light) laser (15 mW) at their absorption maxima and detected in 490 – 550 nm and 575 – 630 nm ranges, respectively. The images (optical sections) were registered using PMT (gain 600, DAPI) or HyD (gain 200, Alexa) working in the integration mode at 16-bit precision. The pixel size was 90 nm in the xy plane and 350 nm along optical axis. The pixel dwell time was 2.5 μs (4x averaging) and the confocal pinhole set to 1 Airy unit (at 530 nm). The cells were imaged at room temperature. The stacks of optical sections (Alexa 488 and 568) were subjected to blind deconvolution (15 iterations) using Huyghens v. 3.7 (SVI, The Netherlands). The processing was initialized with the nominal PSF of the objective and performed at SNR set to 15. The background was estimated as a minimum of average intensity in 25x25 region. Following deconvolution the nuclei (DAPI) were segmented using Otsu thresholding (2 classes). Overlapping nuclei were separated with Euclidean distance transform followed by watershedding. The Alexa 488 and 568 images were summed, processed with median filter (size 7x7x3) and dilated (11x11x3 neighborhood). The cells were segmented using Otsu thresholding and single cell masks were constructed with iterative dilation of the nuclear masks. The dilation steps were ordered by intensity of processed cell images. The volumes corresponding to nuclei were then excluded from the cell masks. Coefficients of intensity correlation (Pearson and Spearman) between intensities of Alexa 488 and 568 images were calculated on cell-by-cell basis, using the respective masks. The operation was repeated using the Alexa 568 images shifted by ±8 voxels in x and y and ±2 voxels in z direction. The respective coefficients were calculated using union of two respective cellular masks and corresponded to random association of Alexa 488 and 568 fluorescence, in a cell. The raw correlation coefficients were then divided by their random counterparts (on cell-by-cell basis) to create standardized Pearson and Spearman values.

Live imaging of microtubule dynamics

For microtubule dynamics analysis, Rat2 cells were electroporated with pEGFP-EB3 or pEGFP-CLIP-170 plasmids. Forty-eight hours later, time-lapse movies of EGFP-EB3 or EGFP-CLIP-170 comets were taken using an Andor Revolutions XD spinning disc microscope with a 63× lens and 1.6 optovar at 1004 × 1002 pixel resolution. Images were taken with an exposure of 200 ms and interval of 0.3 s, collecting a total of 600 frames over 3 min. During imaging, cells were kept in a Chamlide magnetic chamber (Quorum Technologies) at 37°C with 5% CO_2 in the incubator that was part of the microscope system. Only EGFP-EB3 or EGFP-CLIP-170 comets whose movement lasted at least four consecutive frames and had a displacement length of at least 10 pixels were analyzed using the ImageJ "TrackMate" plugin [89]. The reported values are the number of tracks (i.e., the quantification of objects detected as comets), the total run length of comets before catastrophe (*Track Displacement*), comet lifetime (*Track Duration*), and *Track Mean Speed*. For the analysis, values were calculated as means for each cell.

Live imaging of neurons

An Andor Revolutions XD confocal spinning disc microscope and a Chamlide magnetic chamber were used for the *in vivo* imaging of cells. Cell recording was performed at 37°C and 5% CO_2 in a thermostat-controlled incubator. Images were collected using a 63× objective and 1 optovar in the form of a time-lapse movie every second. The total imaging time was 3 min. The images were acquired at 502 × 501 pixel resolution. Individual tracks were obtained manually in ImageJ. Based on these tracks, kymographs were created in ImageJ with the "Kymograph Clear" plugin [90]. By tracing lines on the kymographs, the number of particles that moved at a given time and distance was determined, and their velocity was

calculated by determining the difference between the height of the starting point and end point of a given particle.

Protein production in bacteria and pull-down experiment

Recombinant proteins were produced in the *E. coli* BL21 strain. Individual clones that were transformed with plasmids that encoded proteins of interest were picked from the plates and inoculated to 5 ml of LB with appropriate antibiotic. After overnight cultivation at 37°C with shaking, bacteria were refreshed with new medium in a 1:50 ratio and further cultured until reaching an optical density at 600 nm (OD_{600}) of 06-0.8. Protein production was induced using 1 mM isopropyl-β-D-1-thiogalactopyranoside (IPTG; Carl Roth, catalog no. CN08.3). His_6-AP-2β appendage domain, GST-Eps15, and free GST-tag were produced at 37°C for 2 h, and GST-$p150^{Glued}$ fragments were produced at 21°C overnight. For protein purification, cultures were centrifuged at 4,500 × *g* for 10 min, and the pellet was resuspended in lysis buffer (50 mM Tris [pH, 8.0], 150 mM NaCl, 0.1% Triton X-100, and protease inhibitors). For all subsequent stages, lysates were kept on ice. After resuspension, the cells were lysed by sonication in a Sonics VCX130 PB sonicator (Vibra-Cell) in two 30-s sessions with a 70% amplitude. After sonication, lysates were centrifuged at 13,000 × *g* for 5 min to remove the insoluble fraction. For the pull-down experiment, the bait protein was then added to Glutathione-Sepharose 4B resin (Merck, catalog no. GE17-0756-01) at a ratio of 30 µl beads for each 10 ml of original bacterial culture and incubated for 1 h with end-to-end rotation. After incubation, the resin was washed three times with lysis buffer, and the prey protein lysate was added. After another 1 h of incubation, the resin was again washed three times with lysis buffer and prepared for Western blot by dissolving in 1× Laemmli buffer and incubation in a heat block at 94°C for 15 min.

Whole-cell lysate preparation

For the Western blot analysis of proteins in whole-cell lysates, Rat-2 cells were lysed in lysis buffer (20 mM Tris [pH 7.5], 150 mM NaCl, 2 mM EDTA, 0.5% Triton X-100, 0.5% NP-40, 2 mM $MgCl_2$, and 10% glycerol supplemented with protease and phosphatase inhibitors). The total protein concentration in whole-cell lysates was measured using the Pierce BCA Protein Assay Kit (Thermo Fisher, catalog no. 23225) according to the manufacturer's instructions. Afterward, 4× Laemmli sample buffer was added to the lysates, followed by boiling for 5 min at 95°C.

Immunoprecipitation

For the immunoprecipitation (IP) of endogenous proteins from HEK293T cells, the cells were lysed for 15 min on ice in lysis buffer (20 mM HEPES [pH 7.5], 120 mM KCl, and 0.3% 3-((3-cholamidopropyl) dimethylammonio)-1-propanesulfonate (CHAPS) supplemented with protease and phosphatase inhibitors, in addition to 100 nM rapamycin for variants in which cells were treated with rapamycin) and spun. Next, 2 µg of anti-AP-2β or anti-$p150^{Glued}$ primary antibody or IgG (as a negative control) was added to the supernatant and incubated overnight at 4°C while rotating. The next day, a mix of lysate and antibodies was added to 30 µl of Dynabeads Protein G (Thermo Fisher, catalog no. 10004D) and incubated for 4 h at 4°C while rotating. Beads were then washed four times in wash buffer (20 mM HEPES [pH 7.5], 120 mM KCl, and 0.1% CHAPS), eluted in 2× Laemmli sample buffer, and analyzed by sodium dodecyl sulfate-polyacrylamide gel electrophoresis (SDS-PAGE) followed by Western blot. The IP of AP-2β from rat brain extracts was performed as described previously (Kononenko et al., 2017). For the IP of heterologous proteins, HEK293T cells were transfected with pEGFPC1-Ap2b1, GFP-β-actin-$p150^{Glued}$, or pEGFPC1 (as a negative control). Forty-eight hours after transfection, the cells were lysed for 15 min on ice in lysis buffer (10 mM Tris [pH

7.5], 150 mM NaCl, 0.5 mM EDTA, and 0.15 % CHAPS supplemented with protease and phosphatase inhibitors) and spun using a benchtop centrifuge at maximum speed for 15 min at 4°C. The lysates were then incubated with GFP-Trap Agarose (20 µl per variant; Chromotek, catalog no. gta-10) for 2 h at room temperature, followed by four washes with wash buffer (10 mM Tris [pH 7.5], 150 mM NaCl, and 0.5 mM EDTA). The immunoprecipitated proteins were next used for the mTOR kinase assay.

Avi-tag pull down of in vivo biotinylated proteins and AP-2β-ear binding

His_6-AP-2β appendage domain was produced and induced as it was described in section *Protein production in bacteria.* For protein purification, cultures were centrifuged at 4,500 × *g* for 10 min, and the pellet was resuspended in lysis buffer (50 mM NaH_2PO_4/Na_2HPO_4 pH 8, 300 mM NaCl, 10 mM imidazole, 10% glycerol, 10 mM β-mercaptoethanol 0.1% Triton X-100, and protease inhibitors). For all subsequent stages, lysates were kept on ice. After resuspension, the cells were lysed by sonication in a Sonics VCX130 PB sonicator (Vibra-Cell) in two 25-s sessions with a 70% amplitude. After sonication, lysates were centrifuged at 13,000 × *g* for 5 min to remove the insoluble fraction. The column with 5 ml agarose - Ni - NTA used for affinity chromatography of recombinant protein was equilibrated with 20 ml of lysis buffer and flow rate of approximately 1 ml per minute. Then the cell lysate (obtained from 2 liters of culture) was added to the column with flow rate of approximately 0.5 ml per minute. After the lysate has passed through the column the agarose resin was washed successively with 50 ml of the appropriate buffers: lysis buffer, lysis buffer supplemented with 2 M NaCl and lysis buffer supplemented with 20 mM imidazole. Then the protein was eluted with 25 ml of elution buffer (50 mM NaH_2PO_4/Na_2HPO_4 pH 8, 2 M NaCl, 250 mM imidazole, 10% glycerol, 10 mM β-mercaptoethanol 0.1% Triton X-100). One ml fractions were collected and verified for presence of purified protein. These containg highest amount of His_6-AP-2β ear domain were

pooled and used for binding experiments. M-280 streptavidin Dynabeads (Thermo Fisher, catalog no. 11205D) were incubated for 1 h with blocking buffer (20 mM HEPES [pH 7.5], 120 mM KCl, 0.5 mg/ml BSA, and 20% glycerol). Beads were washed with lysis buffer (20 mM HEPES [pH 7.5], 120 mM KCl, and 0.3% CHAPS supplemented with protease and phosphatase inhibitors). Forty-eight hours after transfection with BirA and plasmids that encoded Avi-tagged proteins, HEK293T cells were lysed for 15 min on ice in lysis buffer and spun using a benchtop centrifuge at maximum speed (15 min, 4°C). The supernatant was added to the previously prepared M-280 streptavidin Dynabeads and incubated together for 1 h at 4°C while rotating. The beads were then washed on ice four times in wash buffer (20 mM HEPES [pH 7.5], 500 mM KCl, and 0.1% CHAPS) and incubated with 0.2 mg/ml His_6-AP-2β ear domain purified from bacteria in binding buffer (20 mM HEPES [pH 7.5], 300 mM KCl, and 0.1% CHAPS) for 2 h at 4°C while rotating. The beads were then washed four times with binding buffer, eluted in 2× Laemmli sample buffer, and analyzed by SDS-PAGE followed by Western blot.

Western blot

Protein samples were analyzed by SDS-PAGE and immunoblotting according to standard laboratory protocols. Primary antibodies that were used for Western blot are listed in Table 1. Proteins of interest were detected using HRP- or IRdye-conjugated secondary antibodies in a chemo-luminescence reaction or with the Odyssey LiCor Biosciences system, respectively. The densitometry analysis of LC3B amount was performed using Image Studio Lite (LiCor Biosciences) and a previously described method (Degasperi et al., [91]. Specifically, the signal intensities for LC3B I and LC3B II were first measured. Based on these values, normalization was performed. First, for all variants in a single replicate, the sum of intensities for a given protein was calculated. Second, individual protein band intensities were

divided by this sum. Such normalization was performed for LC3B I, and LC3B II. Finally having normalized values, the ratio between LC3B II and LC3B I was calculated by dividing the normalized values of LC3B II by LC3B I.

Kinase assays

An *in vitro* phosphorylation assay was performed for 20 min at 30°C in kinase assay reaction buffer (25 mM HEPES [pH 7.5], 50 mM KCl, and 10 mM $MgCl_2$) in the presence of 2.5 μCi [γ-^{33}P]ATP (Hartmann Analytic) and 2.5 mM "cold" ATP using a recombinant, active mTOR kinase fragment (1362-2549 aa; Millipore, catalog no. 14-770) and proteins that were immunoprecipitated from HEK293T cells or commercial mTOR substrate (Merck Millipore, catalog no. 12-645). The reaction was stopped by adding 4× Laemmli sample buffer and boiling for 5 min at 95°C. Next, the samples were separated by SDS-PAGE. The gel was stained with Coomassie Brilliant Blue and dried. The radioactive signal was detected and analyzed using a Typhoon Trio+ Phosphorimager (GE Healthcare).

Statistical analysis

The exact numbers of cells (*n*) that were examined for the respective experiments and number of repetitions of each experiment (*N*) are provided in the figure legends. The statistical analyses were performed using GraphPad Prism 9 software. The Shapiro-Wilk test was used to assess whether the data distribution met the assumptions of a normal distribution. For comparisons between two groups, the *t*-test (in the case of a normal distribution) or Mann-Whitney test (in the case of a non-normal distribution) was used to verify statistical significance. For comparisons between more than two groups, the data were analyzed using one-way analysis of variance (ANOVA) followed by Tukey's multiple-comparison *post hoc* test (in the case of a normal distribution) or the Kruskal-Wallis test and Dunn's multiple-

comparison *post hoc* test (in the case of a non-normal distribution). For comparisons between two factors, the data were analyzed using two-way ANOVA followed by Tukey's multiple-comparison *post hoc* test.

Results

mTORC1 inhibition increases p150^{Glued}–AP-2 interaction and transport along microtubules

Recent work shows that mTOR inhibition increases the biosynthesis of RILP and enhances its recruitment to autophagosomes, potentiating their transport in different cell types, including neurons [45]. This finding prompted us to investigate whether rapamycin, an inhibitor of mTOR complex 1 (mTORC1), also affects the AP-2–dynactin interaction that is responsible for the axonal transport of amphisomes (Kononenko et al., 2017). We performed the immunoprecipitation (IP) of endogenous AP-2β from brain lysates from control rats and rats that were treated with rapamycin for 8 days. Rapamycin treatment efficiently decreased the phosphorylation of ribosomal protein S6 (P-S6) at Ser235/236, confirming efficient mTORC1 inhibition, and increased the co-IP of p150^{Glued} with AP-2β. We observed no noticeable difference in overall levels of p150^{Glued} and AP-2β in corresponding input fractions (**Fig. 1A**).

mTORC1 inhibition potentiates the AP-2–dynactin interaction in the brain. Therefore, we next tested the effects of rapamycin on the retrograde transport of AP-2β and p150^{Glued} in axons of hippocampal neurons. We transfected neurons that were cultured *in vitro* (day *in vitro* 5 [DIV5]) with plasmids that encoded tdTomato-tagged p150^{Glued} and green fluorescent protein (GFP)-tagged AP-2β. Two days later, we imaged the behavior of fluorescently tagged proteins in axons in dimethylsulfoxide (DMSO)-treated (control) cells and cells that were treated with 100 nM rapamycin for 2 h (**Fig. 1B-G**, **Movie 1-4**, **Fig. S1A**). Similarly to the brain tissues, rapamycin decreased P-S6 levels (**Fig. 1B, C**). We also observed a significant increase in the

number of AP-2β/p150^{Glued}-positive objects (**Fig. 1G**), suggesting that mTORC1 inhibition boosted the AP-2–dynactin interaction in neurons, but these objects were largely immobile. At the same time, the difference between fractions of mobile AP-2β/p150^{Glued}-positive objects was statistically nonsignificant under the tested conditions (**Fig. 1F**). AP-2-positive amphisomes carry TrkB receptors. Thus, we analyzed whether AP-2β/p150^{Glued} objects become more mobile upon the treatment of neurons with the TrkB agonist BDNF (**Fig. 1H, I**, **Movie 5-8**, **Fig. S1A**). BDNF treatment significantly enhanced P-S6 immunofluorescence, and rapamycin prevented it, as expected (**Fig. 1B, C**). At the same time, BDNF treatment resulted in significantly more mobile AP-2β/p150^{Glued} particles in cells with mTORC1 inhibition compared with cells that were treated only with BDNF (**Fig. 1J, K**). BDNF and rapamycin had no significant effect on the velocity of the analyzed objects (**Fig. S1B**). Thus, we concluded that mTORC1 inhibition in neurons potentiates the AP-2–dynactin interaction in axons, which results in an increase in the retrograde transport of such complexes upon BDNF treatment.

We next investigated whether mTORC1 inhibition has a similar effect on the co-occurrence of p150^{Glued} and AP-2β in non-neuronal cells using HEK293T and Rat2 cell lines. Under basal culture conditions, there was some evidence of an AP-2–dynactin interaction, demonstrated by IP (HEK293T), immunofluorescence colocalization (Rat2), and the proximity ligation assay (PLA; Rat2) (**Fig. 2; Fig. S2**). The treatment of HEK293T cells with 100 nM rapamycin for 2 h decreased P-S6 levels and increased AP-2β-p150^{Glued} co-IP (**Fig. 2A**). In Rat2 cells, rapamycin decreased S6 phosphorylation (**Fig. 2B**) and enhanced the AP-2β–p150^{Glued} interaction, measured by immunofluorescence signal colocalization analysis and PLA using antibodies against endogenous proteins. Colocalization analysis showed relatively low colocalization under basal conditions and an increase in rapamycin-treated cells (**Fig. S2A-E**). The PLA results additionally confirmed the biochemical and immunofluorescence evidence that is described above (**Fig. 2B-D, Fig. S2F**). AZD-8055, an adenosine triphosphate (ATP)-

competitive inhibitor of mTOR (2 h, 100 nM), also effectively decreased P-S6 immunofluorescence and increased AP-2β–p150^{Glued} PLA signal in Rat2 cells (**Fig. 2B, E, F**), supporting our hypothesis that mTOR inhibition enhances the studied interaction. Further analysis using PLA that was adjusted for electron microscopy (EM) revealed that the AP-2β–p150^{Glued} PLA signal in rapamycin-treated Rat2 cells localized primarily to organelles containing electron dense material characteristic for lysosomes and occasionally in double-membrane organelles, which we classified as autophagosomes. In control, DMSO-treated cells PLA-EM signal could be also spotted, but less frequently and rarely on lysosome-like structures (**Fig. 2G**). Altogether, our results indicate that mTORC1 inhibition enhances the interaction between AP-2 and dynactin in various cell types.

p150^{Glued} interaction with AP-2β is indirect and requires dynactin integrity

Our previous studies [31] and data that are described above show that AP-2β and p150^{Glued} can form a complex that in neurons moves along microtubules, but its further characterization is needed. Therefore, in the following experiments, we first focused on the biochemical characterization of this interaction. Using an Avi-tag pull-down assay, we previously demonstrated that full-length p150^{Glued} that is produced in HEK293T cells can effectively bind the *E. coli*-produced β2 ear of AP-2β [31]. Therefore, we used this system to characterize the p150^{Glued}–β2-ear interaction further and clarified which p150^{Glued} domains are required. We first compared the ability of the N-terminal (1-490 aa; N) and C-terminal (490-end; C) parts of p150^{Glued} and the full-length protein (**Fig. 3A**) that is produced in HEK293T cells to bind the His-tagged β2 ear. The C-terminal part of p150^{Glued} was as effective as the full-length protein, whereas its N-terminus did not bind the AP-2 fragment, exactly like β-galactosidase that served as the negative control (**Fig. 3B**). Moreover, a shorter fragment of the C-terminus (1049-end; C2; **Fig. 3A**), which is known for its contribution to the dynactin

interaction with cargo adaptors [13, 54, 55], also bound the β2 ear (**Fig. 3C**). Notably, however, the newest structural and biochemical data raise the issue of whether the C-terminus of p150^{Glued} binds cargo adaptors directly [10, 11]. Indeed, when both C-terminal fragments of p150^{Glued} were produced in *E. coli*, no interaction with the AP-2β fragment was observed (**Fig. 3D, E**). At the same time, the β2 ear interacted with Eps15 protein (541-790 aa fragment fused to GST; Chi et al., 2008; Keyel et al., 2008), used as a positive control. The most C-terminal part of p150^{Glued} is known for its role in connecting the dynactin sidearm with the Arp-1 rod that binds cargo [16]. Indeed, Western blot indicated that during the p150^{Glued} Avi-tag pull-down, regardless of harsh washing conditions, the dynactin Arp1-rod proteins Arp1 and p62 also co-purified from HEK293T cells (**Fig. 3F**). This suggests that intact dynactin might be involved in formation of the multi-protein complex that contains p150^{Glued} and AP-2β. Indeed, overexpression of the p50 subunit of dynactin, which is routinely used to disrupt dynactin complex integrity by dissociation of the sidearm and Arp1 rod [58, 59]; see **Fig. 3G**), completely blocked the rapamycin-driven increase in p150^{Glued}-AP-2β PLA signal in Rat2 cells (**Fig. 3H, I**). Thus, although p150^{Glued} and AP-2β are unlikely to bind each other directly, their interaction (evident upon mTORC1 inhibition) requires the C-terminus of p150^{Glued} and an undisturbed interaction between the dynactin sidearm and Arp-1 rod.

CLIP-170 is needed for AP-2–dynactin interaction

p150^{Glued} is a +TIP. Therefore, we tested whether the p150^{Glued}–AP-2β interaction requires its ability to target dynamic microtubules. p150^{Glued} microtubule plus-end targeting requires the presence of CLIP-170 [21, 22]. Thus, we tested whether CLIP-170 knockdown impacts the p150^{Glued}–AP-2β interaction. We knocked down CLIP-170 in Rat2 and HEK293T cells using rat- and human-specific siRNAs, respectively, and performed the PLA and IP 72 h later. Both siRNAs against CLIP-170 effectively reduced CLIP-170 levels compared with cells

that were transfected with control siRNAs (**Fig. 4A-C**). At the same time, the loss of CLIP-170 potently prevented the rapamycin-induced p150^{Glued}–AP-2β interaction (**Fig. 4A, D, E**). Of note, CLIP-170 knockdown did not affect overall distribution of AP-2β, both in control and rapamycin treated cells (**Fig. S3A)**.

CLIP-170 knockdown may result, in addition to p150^{Glued} displacement, in substantial changes in microtubule dynamics, especially in cells that do not express CLIP-115 [21]. Although Rat2 cells express both CLIPs (**Fig. 4B**) and our siRNAs do not target CLIP-115, we directly tested effects of CLIP-170 knockdown on microtubule dynamics and the role of microtubule dynamics in the AP-2–dynactin interaction. Indeed, CLIP-170 knockdown had no effect on EB3-GFP mobility that highlights dynamic plus ends of microtubules (**Fig. S3B-F, Movies 9-10**). Next, we performed a p150^{Glued}–AP-2β PLA in Rat2 cells that were treated with 100 nM nocodazole that was added either 15 min before or after rapamycin treatment. At such low concentrations, nocodazole blocks plus-end microtubule dynamics instead of depolymerizing microtubules [60]. Indeed, 1 h of such nocodazole treatment of Rat2 cells already resulted in the loss of EB3-GFP and CLIP-170 comets, confirming the inhibition of microtubule dynamics (**Fig. 4J-O**, **Movies 11-14**). Such treatment did not affect the p150^{Glued}–AP-2β PLA signal under basal conditions or in response to rapamycin treatment (**Fig. 4F-I**). In contrast to nocodazole, rapamycin treatment did not affect EB3-GFP microtubule plus-end tracking behavior (**Fig. S3G-J**, **Movie 15, 16**). Notably, rapamycin did not change the plus-end tracking behavior of CLIP-170–GFP that was overexpressed in Rat2 cells (**Fig. S3K-N**, **Movie 17, 18**). This observation is consistent with our previous data on the lack of effect of rapamycin on endogenous CLIP-170 microtubule binding in neurons and HeLa cells [26].

Overall, the data suggest that microtubule dynamics, at least in the short term, is not needed for the AP-2–dynactin interaction. Low-dose nocodazole treatment should also result in p150^{Glued} displacement from dynamic microtubule plus ends, similar to CLIP-170, but we did

not observe any impact of nocodazole on p150^{Glued}–AP-2 complex formation. Thus, p150^{Glued} displacement from microtubules unlikely explains the effects of CLIP-170 knockdown on the p150^{Glued}–AP-2β PLA interaction. We could confirm this hypothesis using a dominant-negative CLIP-170 mutant that lacks the N-terminal part of the protein and was previously shown to severely affect microtubule dynamics and displace p150^{Glued} from microtubule plus ends [24]. The 48 h overexpression of this protein in Rat2 cells did not prevent the rapamycin-induced increase in the AP-2β–p150^{Glued} PLA signal (**Fig. S3O, P**). In summary, CLIP-170 is needed for the AP-2–dynactin interaction, but two of its canonical functions (i.e., the regulation of microtubule dynamics and targeting p150^{Glued} to microtubule plus ends) do not appear to be directly and immediately involved.

mTORC1-dependent autophagy triggers AP-2–dynactin interaction.

Low mTOR activity affects the dynactin–AP-2 interaction, but the decrease in mTOR-dependent CLIP-170 phosphorylation is likely not involved. Thus, we further searched for the potential mechanism that can explain our observation. We first tested the hypothesis that p150^{Glued} or AP-2β may be a direct substrate of mTOR. *In vitro* kinase assays, using GFP-AP-2β or GFP-p150^{Glued} and the mTOR active fragment, ruled out such a possibility (**Fig. 5A**). Furthermore, inspection of available datasets of mTOR-dependent phosphoproteomes (e.g., Robitaille et al., 2013; Schwarz et al., 2015) did not support the mTOR-dependent phosphorylation of other dynactin subunits. The rapamycin treatment of HEK293T cells (100 nM, 2 h) also did not affect the connection between the dynactin sidearm and its Arp1 rod, indicated by the lack of differences in the co-IP of p150^{Glued} with p62 and Arp1 between analyzed conditions (**Fig. 5B**). Thus, we concluded that the observed effects of mTORC1 inhibition on the AP-2–dynactin interaction are not driven by direct actions of mTOR on the dynactin complex or AP-2β.

In Rat2 cells, EM-PLA revealed organelles that resembled lysosomes as a preferential location of the AP-2–dynactin interaction upon rapamycin (**Fig. 2G**). However, in neurons, AP-2 serves as an adaptor complex for the microtubule transport of LC3-positive amphisomes [31], which arise from the fusion of autophagosomes and late endosomes. But in non-neuronal cells dynein-dynactin-dependent lysosome motility is essential for the completion of autophagocytosis through autophagosome-lysosome fusion [63, 64]. Thus, we investigated whether mTORC1-controlled autophagy under the conditions that were used in the present study is induced and required for the rapamycin-driven AP-2–dynactin interaction. Indeed, treatment with rapamycin decreased the phosphorylation of S6 at Ser235/236, proving mTORC1 inhibition and resulting in an increase in beclin-1 phosphorylation at Ser30, which is an Ulk-1 target and considered an early marker of autophagy (**Fig. 6D**). Furthermore, after 2 h, rapamycin also increased the ratio of the lipidated form of LC3 (LC3B II) to non-lipidated LC3BI, which is routinely used to assess autophagy (**Fig. 6A, B**). Furthermore, rapamycin also increased the formation of large LC3B foci, further confirming autophagy induction (**Fig. 6C**). To verify whether autophagy induction is required for the mTORC1 inhibition-driven AP-2–dynactin interaction, we investigated whether pretreatment with an autophagy initiation inhibitor SBI-0206965 (25 μM; 30 min before rapamycin administration) counteracts the effects of rapamycin. As expected, pretreatment with SBI-0206965 was sufficient to decrease rapamycin-induced beclin-1 phosphorylation at Ser30 and autophagy initiation, imaged using immunofluorescent detection of the formation of endogenous large LC3 foci (**Fig. 6D-F**). Notably, blocking autophagy initiation completely abolished the rapamycin-induced increase in the AP-2-dynactin interaction, measured by IP and PLA in HEK293T cells and Rat2, respectively (**Fig. 6G-I**). Thus, in addition to the presence of CLIP-170, the induction of autophagy is needed for $p150^{Glued}$–AP-2β protein complex formation upon mTORC1 inhibition.

Autophagy initiation is sufficient for AP-2–dynactin interaction.

Our results above show that the initiation of autophagy is essential for the effects of mTORC1 inhibition on AP-2–dynactin complex formation. However, key issue is whether autophagy initiation, even when mTORC1 is active, is sufficient to induce a similar effect. To investigate this possibility, we treated Rat2 cells with L-690330, an inhibitor of inositol monophosphatase and mTOR-independent activator of autophagy [65], and performed an AP-2–dynactin PLA. After 3 h of L-690330 (100 μM) treatment, autophagy level increased, indicated by the LC3BII/LC3BI ratio and formation of large LC3B foci, whereas the level of phosphorylated S6 at Ser235/236 did not decrease as expected (**Fig. 7A-C**). At the same time, this treatment increased the AP-2–dynactin PLA signal similarly to rapamycin treatment (**Fig. 7D, E**). Altogether, our results show that autophagy induction alone is sufficient to induce AP-2–dynactin complex formation. Additionally, as in case of rapamycin treatment, CLIP-170 knockdown blocked the L-690330-induced increase in the AP-2–dynactin interaction (**Fig. 7F-H**). This observation suggested potential novel autophagy-related activities of CLIP-170. Thus, we tested whether CLIP-170 knockdown affects autophagy that is induced by rapamycin or L-690330 and show that the loss of CLIP-170 prevented increase in the LC3BII/LC3BI ratio and LC3 foci formation, caused by both autophagy inducers (**Fig. 7I-K**). These findings suggest that the dynactin interaction with the AP-2 adaptor complex requires contributions from CLIP-170 and autophagy.

Discussion

Recent work demonstrated that AP-2 is an adaptor protein for the dynein-dynactin transport of amphisomes along neuronal axons [29, 31]. To date, however, important questions about mechanistic details of dynactin–AP-2 interaction regulation have not been answered.

Here, we demonstrate that AP-2 and dynactin cooperate in neurons and non-neuronal cells under autophagy-permissive conditions, including, but not restricted to, mTOR inactivation. Furthermore, we show that the co-occurrence of AP-2β with $p150^{Glued}$ does not require binding the latter to microtubule plus ends or microtubule dynamics. However, this interaction requires the presence of CLIP-170 and integrity of the multiprotein dynactin complex.

Autophagy induction but not mTOR inhibition is essential for AP-2–dynactin interaction

The initial finding that stimulated our research was the observation that rapamycin enhances AP-2–dynactin complex formation in neurons. This discovery raised the question of how mTORC1 inhibition stimulates this interaction. The present findings show that AP-2β or $p150^{Glued}$ is not an mTORC1 substrate, instead supporting the scenario that mTORC1 inhibition promotes AP-2–dynactin complex formation indirectly via autophagy initiation (**Fig. 6F-H**). Moreover, the pharmacological induction of autophagy that does not involve mTORC1 inhibition was sufficient to induce this interaction (**Fig. 7F-H**), indicating that the direct trigger for the AP-2–dynactin interaction is autophagy and not mTORC1 inhibition. Furthermore, it explains why the coexistence of AP-2β and $p150^{Glued}$ is readily visible in axons. In non-neuronal cells, it is barely detectable under basal conditions. In cultured neurons, axonal autophagy is relatively high and stable at a steady-state level. Autophagosomes are continuously formed at the axonal growth cone or at presynaptic sites and likely fuse with late endosomes, forming amphisomes, and are transported toward the cell soma [31, 47, 50, 51, 53, 66]. Thus, there is a constant need for AP-2–dynactin complexes in axons to transport amphisomes [31]. However, if axonal autophagy is constitutive and if autophagy is sufficient to drive the AP-2–dynactin interaction, then how does mTORC1 inhibition potentiate it? Although some studies show that mTORC1 inhibition does not increase autophagy in neurons [67, 68], other studies reported that it is nevertheless possible [69, 70]. Such observations show

that this process can still be upregulated, at least under some conditions, despite its relatively high basal level. In contrast to neuronal axons, autophagy in many cultured non-neuronal cells is at a low level under basal conditions, and its induction requires additional stimuli (e.g., mTORC1 inactivation). Consequently, the degree of the AP-2–dynactin interaction in such cells is likely to be adjusted to the current level of autophagy in the cell.

Our results indicate that autophagy is a critical cellular process for the interaction of AP-2 with dynactin. Nevertheless, the PLA-EM results did not identify autophagosomes as the primary AP-2-dynactin interaction site in non-neuronal cells. In this context, important questions are where and for what purpose AP-2-dynactin interaction occurs upon autophagy induction. As mentioned already, in neurons AP-2-dynactin complex is involved in the transport of signaling amphisomes in axons [31]. However, in non-neuronal cells, amphisomes are considered temporary structures [38, 71]. Moreover, our EM findings in Rat2 cells (**Fig. 2G**) revealed an AP-2β–p150^{Glued} PLA signal co-occurring often with lysosomes. The autophagic lysosome reformation (ALR) is a process linking autophagy, lysosomes and AP2 [72]. During ALR, protolysosomes emerge from autolysosomes, resulting from the fusion of mature autophagosomes and lysosomes. Protolysosome formation requires clathrin and AP2 [33]. Protolysosomes mature into lysosomes and can enter the next autophagy cycle. According to Hilverling et al. [73], ALR occurs at the cell's periphery. The recovered lysosomes are next transported to the perinuclear regions. Thus, it is tempting to speculate that AP-2-dynactin interaction occurs on such newly formed lysosomes already possessing AP-2. Since ALR requires autophagy to occur, such a scenario would explain why autophagy is necessary for the appearance of AP-2-dynactin interaction. Yet, ALR requires mTOR activity and, therefore, should not occur in the presence of its inhibitors [74]. Thus, it is unlikely that autophagy-induced interaction of AP-2-dynactin involves ALR. Another process that links autophagy and lysosomes is autolysosome formation mentioned above. Korolchuk et al. [75] showed that

under cell starvation conditions, dynein-dynactin-dependent transport of lysosomes toward the cell nucleus is crucial for their pH regulation and fusion with autophagosomes. Hence, it is a plausible that the recruitment of AP-2-dynactin to lysosomes at the onset of autophagy is designed to ensure the proper fusion of these two organelles at the end of the process. Also, previous studies have shown that the RILP protein is responsible for lysosome transport by dynein-dynactin [76]. This suggests that non-neuronal cells use at least two transport systems for one organelle, as it is in neurons, which use different adaptors for amphisome transport [31, 50, 51]. However, further research is needed to confirm this possibility.

AP-2–dynactin interaction requires intact dynactin and CLIP-170

Our data from Rat2 cells show that p50 overexpression and CLIP-170 knockdown prevented the rapamycin-induced co-occurrence of $p150^{Glued}$ and AP-2β. p50 overexpression dissociates $p150^{Glued}$ from the Arp-1 rod that targets cargo [58, 77]. Thus, AP-2 can associate with $p150^{Glued}$ only when dynactin remains intact with a pointed end, which acts as a cargo-targeting module [15]. Our observation that the *E. coli*-purified $p150^{Glued}$ C-terminus did not interact with the AP-2β ear, while the same fragment that was produced in HEK293T cells and was co-purified with Arp-1 rod components (e.g., Arp-1 and p62) did, further corroborates such a conclusion. These findings also align well with several recent dynactin cryo-EM structures that showed that the $p150^{Glued}$ C-terminus, previously considered an adaptor binding site, was not easily accessible and primarily engaged in an interaction with p50 and the pointed end [10, 11].

The observation that CLIP-170 knockdown prevents the AP-2–dynactin interaction is more challenging to explain. The canonical function of this protein in mammalian cells involves microtubule dynamics regulation, specifically by promoting peripheral microtubule plus-end rescue [24]. However, in cell types that express CLIP-115 (e.g., neurons), CLIP-170

knockdown does not visibly affect microtubule dynamics [21]. Rat2 cells expressed CLIP-115 (**Fig. 4B**). Therefore, changes in microtubule dynamics are an unlikely cause of loss of the AP-2–dynactin interaction upon CLIP-170 knockdown. Moreover, we showed that the application of 100 nM nocodazole, which inhibits microtubule dynamics, either before or after rapamycin treatment, did not affect this interaction (**Fig. 4F-I**). We also showed that rapamycin did not affect microtubule dynamics in any way (**Fig. S3F-M**). CLIP-170 knockdown removes $p150^{Glued}$ from the plus ends of microtubules [21, 22]. Thus, one could speculate that $p150^{Glued}$ binding to microtubule plus ends is essential for the AP-2–dynactin interaction. However, the overexpression of a dominant-negative mutant of CLIP-170 also removes $p150^{Glued}$ from plus ends of microtubules [24] but did not affect the AP-2β–$p150^{Glued}$ PLA results (**Fig. S3N-O**). Another possibility could be that CLIP-170 is physically involved in forming the AP-2–dynactin complex. Although an interaction between CLIP-170 and $p150^{Glued}$ has been shown to be important for "aggregating" dynein-dynactin-attached cargo at tyrosinated microtubule plus ends to increase the effectiveness of transport under certain conditions [23], there have been no reports of the necessity of CLIP-170 for cargo and adaptor binding with dynactin. Additionally, the loss of CLIP-170 does not affect the distribution or transport of a variety of dynactin cargos [21, 22].

Considering the above, we hypothesized that CLIP-170 knockdown affects the AP-2–dynactin interaction indirectly by regulating autophagy. Our observation that autophagy is sufficient to induce the AP-2–dynactin interaction in non-neuronal cells supports this hypothesis. Indeed, we present evidence that CLIP-170 knockdown in Rat2 cells lowers the LC3BII/LC3BI ratio in rapamycin and L-690330 treated cells. However, one unresolved issue is how CLIP-170 contributes to this process. Microtubule dynamics and the loss of $p150^{Glued}$ from microtubule plus ends unlikely play essential roles, precisely for the aforementioned reasons. However, there is evidence that the absence of CLIP-170, even when microtubule

dynamics is preserved, disrupts the localization of proteins other than p150^{Glued}. Notably, Lewkowicz et al. [78] showed that CLIP-170 is important for mDia1 positioning at sites of phagocytosis, which is required for actin polymerization and the progression of this process. Other CLIP-170 interactors, such as IQGAP1 [26], also regulate actin polymerization (Brandt and Grosse, 2007; Le Clainche et al., 2007; La Clainche et al., 2007; Brandt et al., 2007). Actin cytoskeleton depolymerization prevents autophagosome formation [81]. Thus, one speculation is that CLIP-170 knockdown leads directly to the mispositioning of proteins that are critical for autophagy, analogical to the loss of mDia1 from phagocytosis sites. Alternatively, the lack of CLIP-170 may affect autophagy via actin polymerization dysregulation at autophagosome initiation sites. Meunier et al. [82] also showed that amphiphysin 2, a protein that is essential for membrane tubulation, interacts with CLIP-170. The loss of CLIP-170 results in the disappearance of membrane tubules, structures that are formed in many events during membrane trafficking. Thus, the loss of CLIP-170 could affect autophagy indirectly by causing membrane dynamics problems that would eventually result in perturbances in the delivery of proteins and membranes that are needed for its initiation or progression. Notably, however, Meunier et al. [82] used HeLa cells that did not express CLIP-115 [21], so the effects of CLIP-170 knockdown would affect microtubule dynamics, unlike in Rat2 cells that were used herein. Thus, determining precisely how CLIP-170 regulates autophagy will likely inspire further studies.

In summary, our study provides new insights into the mechanisms that regulate formation of the dynactin–AP-2 complex, which is essential for the transport of specific cargos, such as autophagosomes, along microtubules. Importantly, we showed that autophagy initiation is necessary and sufficient to trigger the formation of this complex. This finding exemplifies a basic mechanism that allows the coordination of various elements that are involved in a vital cellular process.

Acknowledgments

The authors thank Dr. Anna Akhmanova, Dr. Hong Cao, Dr. Casper Hoogenraad, Dr. Mark McNiven, Dr. Lukasz Swiech and Dr. Agata Zieba-Wicher for the reagents, Dr. Rafaella de Pace, Dr. Carlos Guardia and Dr. Juan Bonifacino for their support with establishing the protocol for the live imaging of neurons, Dr. Katarzyna Poleszak for help with establishing protein production protocols and Dr. Alexander Heberle for help with analyzing existing mTOR phosphoproteome datasets. In addition, we are grateful for comments and discussions to Dr. Iwona Ciechomska, Dr. Kathrin Thedieck and Dr. Viktor Korolchuk. We also thank Alina Zielinska and Marek Sarnacki from our laboratory and Tomasz Wegierski from the Microscopy and Flow Cytometry Core Facility at IIMCB for technical assistance and support, Angelika Jocek for laboratory management logistics, and Michael Arends for proofreading the manuscript.

Funding Statement

Research was supported by Polish National Science Centre Opus grant no. 2016/21/B/NZ3/03639 to JJ. AT was partly financed by Polish National Science Centre Opus grant no. 2017/25/N/NZ3/01280 and 2017/27/B/NZ3/01358. JJ was partly financed by the TEAM grant from the Foundation for Polish Science (POIR.04.04.00-00-5CBE/17-00). AM was partly financed within the Parent-Bridge program of the Foundation for Polish Science, co-financed by the European Union under the European Regional Development Fund (POMOST/2013-7/10) and by I.3.4 Action of the Excellence Initiative - Research University Programme at the University of Warsaw.

Authors Contributions

AT, KB, AB, JW, AM, and JJ designed the experiments. AT, KB, AB, JW, MM, AL, MC-K, TB, AAS, MB, and AM performed the experiments. AT, KB, AB, JW, MM, TB, MB, TR, AM, and JJ analyzed the data. AT, KB, AB, JW, AM, and JJ wrote the manuscript.

Conflict of Interest

None of the authors have any financial or non-financial competing interests.

Data availability

All data generated or analyzed during this study are included in this published article and its supplementary materials. Raw data of all quantitatively analyzed experiments are available from the corresponding author on reasonable request.

References

1. Britt DJ, Farías GG, Guardia CM, Bonifacino JS (2016) Mechanisms of Polarized Organelle Distribution in Neurons. Front Cell Neurosci 10:88. https://doi.org/10.3389/fncel.2016.00088

2. Maday S, Twelvetrees AE, Moughamian AJ, Holzbaur ELF (2014) Axonal transport: cargo-specific mechanisms of motility and regulation. Neuron 84:292–309. https://doi.org/10.1016/j.neuron.2014.10.019

3. Desai A, Mitchison TJ (1997) Microtubule polymerization dynamics. Annu Rev Cell Dev Biol 13:83–117. https://doi.org/10.1146/annurev.cellbio.13.1.83

4. Hirokawa N, Noda Y, Tanaka Y, Niwa S (2009) Kinesin superfamily motor proteins and intracellular transport. Nat Rev Mol Cell Biol 10:682–696. https://doi.org/10.1038/nrm2774

5. Schroer TA (2004) Dynactin. Annu Rev Cell Dev Biol 20:759–779. https://doi.org/10.1146/annurev.cellbio.20.012103.094623

6. Höök P, Vallee RB (2006) The dynein family at a glance. Journal of Cell Science 119:4369–4371. https://doi.org/10.1242/jcs.03176

7. Reck-Peterson SL, Redwine WB, Vale RD, Carter AP (2018) The cytoplasmic dynein transport machinery and its many cargoes. Nat Rev Mol Cell Biol 19:382–398. https://doi.org/10.1038/s41580-018-0004-3

8. Moughamian AJ, Osborn GE, Lazarus JE, Maday S, Holzbaur ELF (2013) Ordered recruitment of dynactin to the microtubule plus-end is required for efficient initiation of retrograde axonal transport. J Neurosci 33:13190–13203. https://doi.org/10.1523/JNEUROSCI.0935-13.2013

9. Ross JL, Wallace K, Shuman H, Goldman YE, Holzbaur ELF (2006) Processive bidirectional motion of dynein-dynactin complexes in vitro. Nat Cell Biol 8:562–570. https://doi.org/10.1038/ncb1421

10. Chowdhury S, Ketcham SA, Schroer TA, Lander GC (2015) Structural organization of the dynein-dynactin complex bound to microtubules. Nat Struct Mol Biol 22:345–347. https://doi.org/10.1038/nsmb.2996

11. Urnavicius L, Zhang K, Diamant AG, Motz C, Schlager MA, Yu M, Patel NA, Robinson CV, Carter AP (2015) The structure of the dynactin complex and its interaction with dynein. Science 347:1441–1446. https://doi.org/10.1126/science.aaa4080

12. Carter AP, Diamant AG, Urnavicius L (2016) How dynein and dynactin transport cargos: a structural perspective. Current Opinion in Structural Biology 37:62–70. https://doi.org/10.1016/j.sbi.2015.12.003

13. Fu M, Holzbaur ELF (2014) Integrated regulation of motor-driven organelle transport by scaffolding proteins. Trends Cell Biol 24:564–574. https://doi.org/10.1016/j.tcb.2014.05.002

14. Hoogenraad CC, Akhmanova A (2016) Bicaudal D Family of Motor Adaptors: Linking Dynein Motility to Cargo Binding. Trends Cell Biol 26:327–340. https://doi.org/10.1016/j.tcb.2016.01.001

15. Yeh T-Y, Quintyne NJ, Scipioni BR, Eckley DM, Schroer TA (2012) Dynactin's pointed-end complex is a cargo-targeting module. Mol Biol Cell 23:3827–3837. https://doi.org/10.1091/mbc.E12-07-0496

16. Saito K, Murayama T, Hata T, Kobayashi T, Shibata K, Kazuno S, Fujimura T, Sakurai T, Toyoshima YY (2020) Conformational diversity of dynactin sidearm and domain organization of its subunit p150. MBoC 31:1218–1231. https://doi.org/10.1091/mbc.E20-01-0031

17. Galjart N (2005) CLIPs and CLASPs and cellular dynamics. Nat Rev Mol Cell Biol 6:487–498. https://doi.org/10.1038/nrm1664

18. Jaworski J, Hoogenraad CC, Akhmanova A (2008) Microtubule plus-end tracking proteins in differentiated mammalian cells. Int J Biochem Cell Biol 40:619–37. https://doi.org/10.1016/j.biocel.2007.10.015

19. Perez F, Diamantopoulos GS, Stalder R, Kreis TE (1999) CLIP-170 highlights growing microtubule ends in vivo. Cell 96:517–27

20. Vaughan KT, Tynan SH, Faulkner NE, Echeverri CJ, Vallee RB (1999) Colocalization of cytoplasmic dynein with dynactin and CLIP-170 at microtubule distal ends. J Cell Sci 112 (Pt 10):1437–1447. https://doi.org/10.1242/jcs.112.10.1437

21. Lansbergen G, Komarova Y, Modesti M, Wyman C, Hoogenraad CC, Goodson HV, Lemaitre RP, Drechsel DN, van Munster E, Gadella TW Jr, Grosveld F, Galjart N, Borisy GG, Akhmanova A (2004) Conformational changes in CLIP-170 regulate its binding to microtubules and dynactin localization. J Cell Biol 166:1003–14. https://doi.org/10.1083/jcb.200402082

22. Watson P, Stephens DJ (2006) Microtubule plus-end loading of p150(Glued) is mediated by EB1 and CLIP-170 but is not required for intracellular membrane traffic in mammalian cells. J Cell Sci 119:2758–2767. https://doi.org/10.1242/jcs.02999

23. Nirschl JJ, Magiera MM, Lazarus JE, Janke C, Holzbaur ELF (2016) α-Tubulin Tyrosination and CLIP-170 Phosphorylation Regulate the Initiation of Dynein-Driven Transport in Neurons. Cell Rep 14:2637–2652. https://doi.org/10.1016/j.celrep.2016.02.046

24. Komarova YA, Akhmanova AS, Kojima S, Galjart N, Borisy GG (2002) Cytoplasmic linker proteins promote microtubule rescue in vivo. J Cell Biol 159:589–99. https://doi.org/10.1083/jcb.200208058

25. Fukata M, Watanabe T, Noritake J, Nakagawa M, Yamaga M, Kuroda S, Matsuura Y, Iwamatsu A, Perez F, Kaibuchi K (2002) Rac1 and Cdc42 capture microtubules through IQGAP1 and CLIP-170. Cell 109:873–85

26. Swiech L, Blazejczyk M, Urbanska M, Pietruszka P, Dortland BR, Malik AR, Wulf PS, Hoogenraad CC, Jaworski J (2011) CLIP-170 and IQGAP1 Cooperatively Regulate Dendrite Morphology. J Neurosci 31:4555–68. https://doi.org/10.1523/JNEUROSCI.6582-10.2011

27. Collins BM, McCoy AJ, Kent HM, Evans PR, Owen DJ (2002) Molecular architecture and functional model of the endocytic AP2 complex. Cell 109:523–535

28. Traub LM (2003) Sorting it out: AP-2 and alternate clathrin adaptors in endocytic cargo selection. J Cell Biol 163:203–8. https://doi.org/10.1083/jcb.200309175

29. Bera S, Camblor-Perujo S, Calleja Barca E, Negrete-Hurtado A, Racho J, De Bruyckere E, Wittich C, Ellrich N, Martins S, Adjaye J, Kononenko NL (2020) AP-2 reduces amyloidogenesis by promoting BACE1 trafficking and degradation in neurons. EMBO Rep 21:e47954. https://doi.org/10.15252/embr.201947954

30. Imai K, Hao F, Fujita N, Tsuji Y, Oe Y, Araki Y, Hamasaki M, Noda T, Yoshimori T (2016) Atg9A trafficking through the recycling endosomes is required for autophagosome formation. J Cell Sci 129:3781–3791. https://doi.org/10.1242/jcs.196196

31. Kononenko NL, Claßen GA, Kuijpers M, Puchkov D, Maritzen T, Tempes A, Malik AR, Skalecka A, Bera S, Jaworski J, Haucke V (2017) Retrograde transport of TrkB-containing autophagosomes via the adaptor AP-2 mediates neuronal complexity and prevents neurodegeneration. Nat Commun 8:14819. https://doi.org/10.1038/ncomms14819

32. Popovic D, Dikic I (2014) TBC1D5 and the AP2 complex regulate ATG9 trafficking and initiation of autophagy. EMBO Rep 15:392–401. https://doi.org/10.1002/embr.201337995

33. Rong Y, Liu M, Ma L, Du W, Zhang H, Tian Y, Cao Z, Li Y, Ren H, Zhang C, Li L, Chen S, Xi J, Yu L (2012) Clathrin and phosphatidylinositol-4,5-bisphosphate regulate autophagic lysosome reformation. Nat Cell Biol 14:924–934. https://doi.org/10.1038/ncb2557

34. Tian Y, Chang JC, Fan EY, Flajolet M, Greengard P (2013) Adaptor complex AP2/PICALM, through interaction with LC3, targets Alzheimer's APP-CTF for terminal degradation via autophagy. Proc Natl Acad Sci USA 110:17071–17076. https://doi.org/10.1073/pnas.1315110110

35. Dikic I, Elazar Z (2018) Mechanism and medical implications of mammalian autophagy. Nat Rev Mol Cell Biol 19:349–364. https://doi.org/10.1038/s41580-018-0003-4

36. Levine B, Klionsky DJ (2004) Development by self-digestion: molecular mechanisms and biological functions of autophagy. Dev Cell 6:463–477

37. Yin Z, Pascual C, Klionsky D (2016) Autophagy: machinery and regulation. Microb Cell 3:588–596. https://doi.org/10.15698/mic2016.12.546

38. Zhao YG, Codogno P, Zhang H (2021) Machinery, regulation and pathophysiological implications of autophagosome maturation. Nat Rev Mol Cell Biol 22:733–750. https://doi.org/10.1038/s41580-021-00392-4

39. Jung CH, Ro S-H, Cao J, Otto NM, Kim D-H (2010) mTOR regulation of autophagy. FEBS Lett 584:1287–1295. https://doi.org/10.1016/j.febslet.2010.01.017

40. Russell RC, Yuan H-X, Guan K-L (2014) Autophagy regulation by nutrient signaling. Cell Res 24:42–57. https://doi.org/10.1038/cr.2013.166

41. Ganley IG, Lam DH, Wang J, Ding X, Chen S, Jiang X (2009) ULK1.ATG13.FIP200 complex mediates mTOR signaling and is essential for autophagy. J Biol Chem 284:12297–12305. https://doi.org/10.1074/jbc.M900573200

42. Hosokawa N, Hara T, Kaizuka T, Kishi C, Takamura A, Miura Y, Iemura S, Natsume T, Takehana K, Yamada N, Guan J-L, Oshiro N, Mizushima N (2009) Nutrient-dependent mTORC1 association with the ULK1-Atg13-FIP200 complex required for autophagy. Mol Biol Cell 20:1981–1991. https://doi.org/10.1091/mbc.E08-12-1248

43. Huang H, Ouyang Q, Zhu M, Yu H, Mei K, Liu R (2021) mTOR-mediated phosphorylation of VAMP8 and SCFD1 regulates autophagosome maturation. Nat Commun 12:6622. https://doi.org/10.1038/s41467-021-26824-5

44. Jung CH, Jun CB, Ro SH, Kim YM, Otto NM, Cao J, Kundu M, Kim DH (2009) ULK-Atg13-FIP200 complexes mediate mTOR signaling to the autophagy machinery. Mol Biol Cell 20:1992–2003. https://doi.org/10.1091/mbc.E08-12-1249

45. Khobrekar NV, Quintremil S, Dantas TJ, Vallee RB (2020) The Dynein Adaptor RILP Controls Neuronal Autophagosome Biogenesis, Transport, and Clearance. Dev Cell 53:141-153.e4. https://doi.org/10.1016/j.devcel.2020.03.011

46. Kim Y-M, Jung CH, Seo M, Kim EK, Park J-M, Bae SS, Kim D-H (2015) mTORC1 phosphorylates UVRAG to negatively regulate autophagosome and endosome maturation. Mol Cell 57:207–218. https://doi.org/10.1016/j.molcel.2014.11.013

47. Cason SE, Carman PJ, Van Duyne C, Goldsmith J, Dominguez R, Holzbaur ELF (2021) Sequential dynein effectors regulate axonal autophagosome motility in a maturation-dependent pathway. J Cell Biol 220:e202010179. https://doi.org/10.1083/jcb.202010179

48. Kimura S, Noda T, Yoshimori T (2008) Dynein-dependent movement of autophagosomes mediates efficient encounters with lysosomes. Cell Struct Funct 33:109–122. https://doi.org/10.1247/csf.08005

49. Stavoe AKH, Holzbaur ELF (2019) Autophagy in Neurons. Annu Rev Cell Dev Biol 35:477–500. https://doi.org/10.1146/annurev-cellbio-100818-125242

50. Andres-Alonso M, Ammar MR, Butnaru I, Gomes GM, Acuña Sanhueza G, Raman R, Yuanxiang P, Borgmeyer M, Lopez-Rojas J, Raza SA, Brice N, Hausrat TJ, Macharadze T, Diaz-Gonzalez S, Carlton M, Failla AV, Stork O, Schweizer M, Gundelfinger ED, Kneussel M, Spilker C, Karpova A, Kreutz MR (2019) SIPA1L2 controls trafficking and local signaling of TrkB-containing amphisomes at presynaptic terminals. Nat Commun 10:5448. https://doi.org/10.1038/s41467-019-13224-z

51. Cheng X-T, Zhou B, Lin M-Y, Cai Q, Sheng Z-H (2015) Axonal autophagosomes recruit dynein for retrograde transport through fusion with late endosomes. J Cell Biol 209:377–386. https://doi.org/10.1083/jcb.201412046

52. Fu M-M, Nirschl JJ, Holzbaur ELF (2014) LC3 binding to the scaffolding protein JIP1 regulates processive dynein-driven transport of autophagosomes. Dev Cell 29:577–590. https://doi.org/10.1016/j.devcel.2014.04.015

53. Maday S, Wallace KE, Holzbaur ELF (2012) Autophagosomes initiate distally and mature during transport toward the cell soma in primary neurons. J Cell Biol 196:407–417. https://doi.org/10.1083/jcb.201106120

54. Hong Z, Yang Y, Zhang C, Niu Y, Li K, Zhao X, Liu J-J (2009) The retromer component SNX6 interacts with dynactin p150(Glued) and mediates endosome-to-TGN transport. Cell Res 19:1334–1349. https://doi.org/10.1038/cr.2009.130

55. Johansson M, Rocha N, Zwart W, Jordens I, Janssen L, Kuijl C, Olkkonen VM, Neefjes J (2007) Activation of endosomal dynein motors by stepwise assembly of Rab7-RILP-p150Glued, ORP1L, and the receptor betalll spectrin. J Cell Biol 176:459–471. https://doi.org/10.1083/jcb.200606077

56. Chi S, Cao H, Chen J, McNiven MA (2008) Eps15 mediates vesicle trafficking from the trans-Golgi network via an interaction with the clathrin adaptor AP-1. Mol Biol Cell 19:3564–3575. https://doi.org/10.1091/mbc.e07-10-0997

57. Keyel PA, Thieman JR, Roth R, Erkan E, Everett ET, Watkins SC, Heuser JE, Traub LM (2008) The AP-2 Adaptor β2 Appendage Scaffolds Alternate Cargo Endocytosis. MBoC 19:5309–5326. https://doi.org/10.1091/mbc.e08-07-0712

58. Cheong FKY, Feng L, Sarkeshik A, Yates JR, Schroer TA (2014) Dynactin integrity depends upon direct binding of dynamitin to Arp1. Mol Biol Cell 25:2171–2180. https://doi.org/10.1091/mbc.E14-03-0842

59. Echeverri CJ, Paschal BM, Vaughan KT, Vallee RB (1996) Molecular characterization of the 50-kD subunit of dynactin reveals function for the complex in chromosome alignment and spindle organization during mitosis. J Cell Biol 132:617–633. https://doi.org/10.1083/jcb.132.4.617

60. Jaworski J, Kapitein LC, Gouveia SM, Dortland BR, Wulf PS, Grigoriev I, Camera P, Spangler SA, Di Stefano P, Demmers J, Krugers H, Defilippi P, Akhmanova A, Hoogenraad CC (2009) Dynamic microtubules regulate dendritic spine morphology and synaptic plasticity. Neuron 61:85–100. https://doi.org/10.1016/j.neuron.2008.11.013

61. Robitaille AM, Christen S, Shimobayashi M, Cornu M, Fava LL, Moes S, Prescianotto-Baschong C, Sauer U, Jenoe P, Hall MN (2013) Quantitative phosphoproteomics reveal mTORC1 activates de novo pyrimidine synthesis. Science 339:1320–3. https://doi.org/10.1126/science.1228771

62. Schwarz JJ, Wiese H, Tölle RC, Zarei M, Dengjel J, Warscheid B, Thedieck K (2015) Functional Proteomics Identifies Acinus L as a Direct Insulin- and Amino Acid-Dependent Mammalian Target of Rapamycin Complex 1 (mTORC1) Substrate. Mol Cell Proteomics 14:2042–2055. https://doi.org/10.1074/mcp.M114.045807

63. Korolchuk VI, Rubinsztein DC (2011) Regulation of autophagy by lysosomal positioning. Autophagy 7:927–928. https://doi.org/10.4161/auto.7.8.15862

64. Pu J, Guardia CM, Keren-Kaplan T, Bonifacino JS (2016) Mechanisms and functions of lysosome positioning. J Cell Sci 129:4329–4339. https://doi.org/10.1242/jcs.196287

65. Sarkar S, Floto RA, Berger Z, Imarisio S, Cordenier A, Pasco M, Cook LJ, Rubinsztein DC (2005) Lithium induces autophagy by inhibiting inositol monophosphatase. J Cell Biol 170:1101–1111. https://doi.org/10.1083/jcb.200504035

66. Maday S, Holzbaur ELF (2014) Autophagosome biogenesis in primary neurons follows an ordered and spatially regulated pathway. Dev Cell 30:71–85. https://doi.org/10.1016/j.devcel.2014.06.001

67. Fox JH, Connor T, Chopra V, Dorsey K, Kama JA, Bleckmann D, Betschart C, Hoyer D, Frentzel S, Difiglia M, Paganetti P, Hersch SM (2010) The mTOR kinase inhibitor Everolimus decreases S6 kinase phosphorylation but fails to reduce mutant huntingtin levels in brain and is not neuroprotective in the R6/2 mouse model of Huntington's disease. Mol Neurodegener 5:26. https://doi.org/10.1186/1750-1326-5-26

68. Tsvetkov AS, Miller J, Arrasate M, Wong JS, Pleiss MA, Finkbeiner S (2010) A small-molecule scaffold induces autophagy in primary neurons and protects against toxicity in a Huntington disease model. Proc Natl Acad Sci U S A 107:16982–16987. https://doi.org/10.1073/pnas.1004498107

69. Boland B, Kumar A, Lee S, Platt FM, Wegiel J, Yu WH, Nixon RA (2008) Autophagy induction and autophagosome clearance in neurons: relationship to autophagic pathology in Alzheimer's disease. J Neurosci 28:6926–6937. https://doi.org/10.1523/JNEUROSCI.0800-08.2008

70. Hernandez D, Torres CA, Setlik W, Cebrián C, Mosharov EV, Tang G, Cheng H-C, Kholodilov N, Yarygina O, Burke RE, Gershon M, Sulzer D (2012) Regulation of presynaptic neurotransmission by macroautophagy. Neuron 74:277–284. https://doi.org/10.1016/j.neuron.2012.02.020

71. Ganesan D, Cai Q (2021) Understanding amphisomes. Biochem J 478:1959–1976. https://doi.org/10.1042/BCJ20200917

72. Chen Y, Yu L (2017) Recent progress in autophagic lysosome reformation. Traffic 18:358–361. https://doi.org/10.1111/tra.12484

73. Hilverling A, Szegö EM, Dinter E, Cozma D, Saridaki T, Falkenburger BH (2022) Maturing Autophagosomes are Transported Towards the Cell Periphery. Cell Mol Neurobiol 42:155–171. https://doi.org/10.1007/s10571-021-01116-0

74. Yu L, McPhee CK, Zheng L, Mardones GA, Rong Y, Peng J, Mi N, Zhao Y, Liu Z, Wan F, Hailey DW, Oorschot V, Klumperman J, Baehrecke EH, Lenardo MJ (2010) Termination of autophagy and reformation of lysosomes regulated by mTOR. Nature 465:942–946. https://doi.org/10.1038/nature09076

75. Korolchuk VI, Saiki S, Lichtenberg M, Siddiqi FH, Roberts EA, Imarisio S, Jahreiss L, Sarkar S, Futter M, Menzies FM, O'Kane CJ, Deretic V, Rubinsztein DC (2011) Lysosomal positioning coordinates cellular nutrient responses. Nat Cell Biol 13:453–460. https://doi.org/10.1038/ncb2204

76. Jordens I, Fernandez-Borja M, Marsman M, Dusseljee S, Janssen L, Calafat J, Janssen H, Wubbolts R, Neefjes J (2001) The Rab7 effector protein RILP controls lysosomal transport by inducing the recruitment of dynein-dynactin motors. Curr Biol 11:1680–1685

77. Jacquot G, Maidou-Peindara P, Benichou S (2010) Molecular and functional basis for the scaffolding role of the p50/dynamitin subunit of the microtubule-associated dynactin complex. J Biol Chem 285:23019–23031. https://doi.org/10.1074/jbc.M110.100602

78. Lewkowicz E, Herit F, Le Clainche C, Bourdoncle P, Perez F, Niedergang F (2008) The microtubule-binding protein CLIP-170 coordinates mDia1 and actin reorganization during CR3-mediated phagocytosis. J Cell Biol 183:1287–98. https://doi.org/10.1083/jcb.200807023

79. Brandt DT, Grosse R (2007) Get to grips: steering local actin dynamics with IQGAPs. EMBO Rep 8:1019–23. https://doi.org/10.1038/sj.embor.7401089

80. Le Clainche C, Schlaepfer D, Ferrari A, Klingauf M, Grohmanova K, Veligodskiy A, Didry D, Le D, Egile C, Carlier MF, Kroschewski R (2007) IQGAP1 stimulates actin assembly through the N-WASP-Arp2/3 pathway. J Biol Chem 282:426–35. https://doi.org/10.1074/jbc.M607711200

81. Aguilera MO, Berón W, Colombo MI (2012) The actin cytoskeleton participates in the early events of autophagosome formation upon starvation induced autophagy. Autophagy 8:1590–1603. https://doi.org/10.4161/auto.21459

82. Meunier B, Quaranta M, Daviet L, Hatzoglou A, Leprince C (2009) The membrane-tubulating potential of amphiphysin 2/BIN1 is dependent on the microtubule-binding cytoplasmic linker protein 170 (CLIP-170). Eur J Cell Biol 88:91–102. https://doi.org/10.1016/j.ejcb.2008.08.006

83. Malik AR, Urbanska M, Gozdz A, Swiech LJ, Nagalski A, Perycz M, Blazejczyk M, Jaworski J (2013) CYR61, a matricellular protein, is needed for dendritic arborization of hippocampal neurons. J Biol Chem. https://doi.org/10.1074/jbc.M112.411629

84. de Boer E, Rodriguez P, Bonte E, Krijgsveld J, Katsantoni E, Heck A, Grosveld F, Strouboulis J (2003) Efficient biotinylation and single-step purification of tagged transcription factors in mammalian cells and transgenic mice. Proc Natl Acad Sci U S A 100:7480–5. https://doi.org/10.1073/pnas.1332608100

85. Urbanska AS, Janusz-Kaminska A, Switon K, Hawthorne AL, Perycz M, Urbanska M, Bassell GJ, Jaworski J (2017) ZBP1 phosphorylation at serine 181 regulates its dendritic transport and the development of dendritic trees of hippocampal neurons. Sci Rep 7:1876. https://doi.org/10.1038/s41598-017-01963-2

86. Koscielny A, Malik AR, Liszewska E, Zmorzynska J, Tempes A, Tarkowski B, Jaworski J (2018) Adaptor Complex 2 Controls Dendrite Morphology via mTOR-Dependent Expression of GluA2. Mol Neurobiol 55:1590–1606. https://doi.org/10.1007/s12035-017-0436-3

87. Hoogenraad CC, Akhmanova A, Howell SA, Dortland BR, De Zeeuw CI, Willemsen R, Visser P, Grosveld F, Galjart N (2001) Mammalian Golgi-associated Bicaudal-D2 functions in the dynein-dynactin pathway by interacting with these complexes. EMBO J 20:4041–4054. https://doi.org/10.1093/emboj/20.15.4041

88. Hoogenraad CC, Akhmanova A, Grosveld F, De Zeeuw CI, Galjart N (2000) Functional analysis of CLIP-115 and its binding to microtubules. J Cell Sci 113 (Pt 12):2285–97

89. Tinevez J-Y, Perry N, Schindelin J, Hoopes GM, Reynolds GD, Laplantine E, Bednarek SY, Shorte SL, Eliceiri KW (2017) TrackMate: An open and extensible platform for single-particle tracking. Methods 115:80–90. https://doi.org/10.1016/j.ymeth.2016.09.016

90. Mangeol P, Prevo B, Peterman EJG (2016) KymographClear and KymographDirect: two tools for the automated quantitative analysis of molecular and cellular dynamics using kymographs. Mol Biol Cell 27:1948–1957. https://doi.org/10.1091/mbc.E15-06-0404

91. Degasperi A, Birtwistle MR, Volinsky N, Rauch J, Kolch W, Kholodenko BN (2014) Evaluating strategies to normalise biological replicates of Western blot data. PLoS One 9:e87293. https://doi.org/10.1371/journal.pone.0087293

Figures

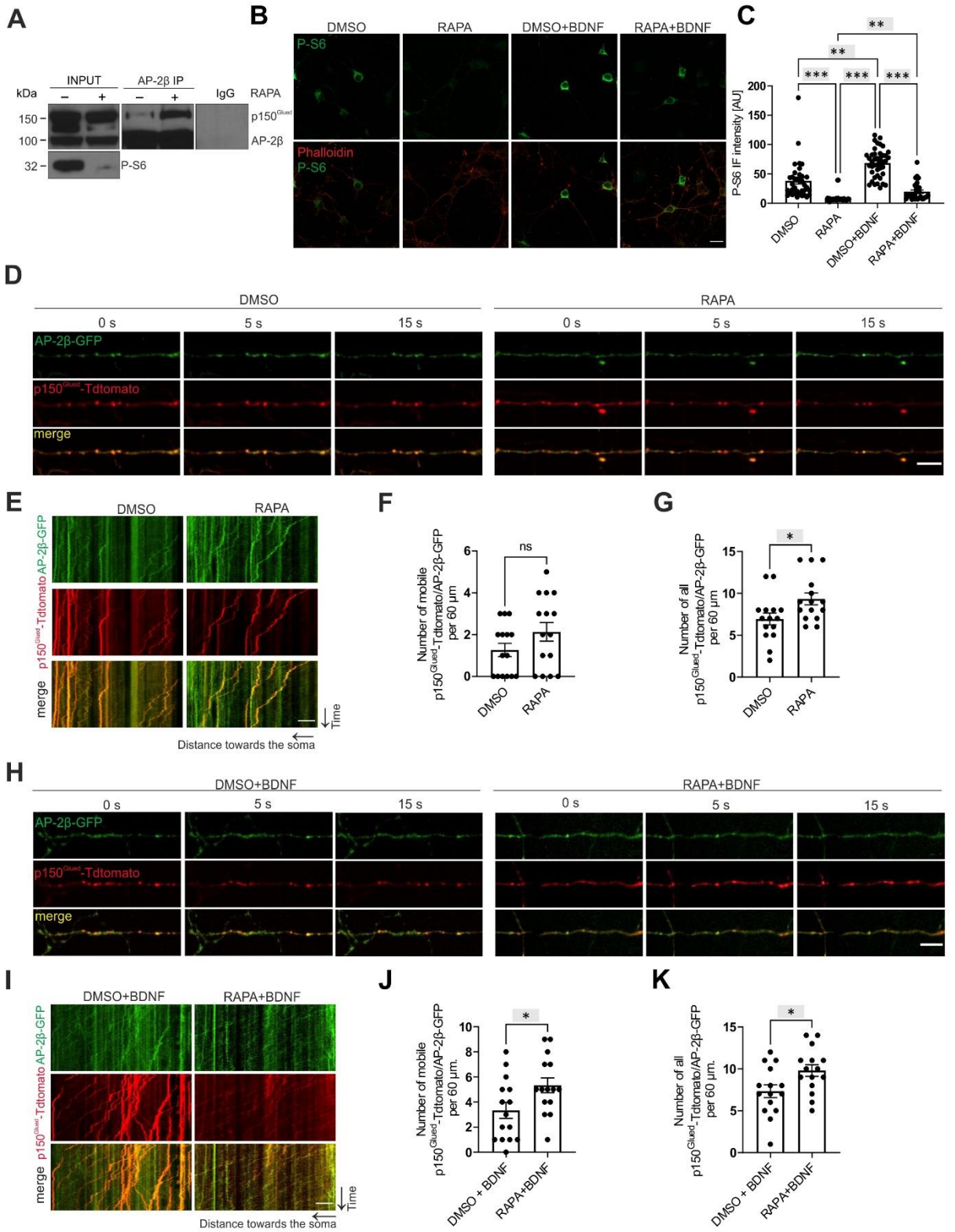

Fig. 1. mTORC1 inhibition in neurons increases p150^{Glued}–AP-2 interaction and transport along axonal microtubules. (A) Western blot analysis of levels of endogenous

p150^{Glued}, AP-2β, P-S6 (Ser235/236), and co-immunoprecipitation of endogenous AP-2β with p150^{Glued} from brain lysates from rats that were treated with rapamycin (RAPA+) or vehicle (RAPA-). INPUT, 10% of lysate used for immunoprecipitation. Shown is a representative example from N = 3 independent experiments. (**B**) Representative pictures of DIV7 neurons that were treated as indicated and immunofluorescently labeled for endogenous P-S6 (Ser235/236) (green) and Alexa Fluor 568 phalloidin. Scale bar = 20 μm. (**C**) Quantification of P-S6 (Ser235/236) immunofluorescence level in cell bodies of neurons that were treated as in J. The data are expressed as the mean fluorescence intensity ± SEM. N = 2 independent experiments. n = 36 cells (DMSO), 39 cells (RAPA), 42 cells (DMSO+BDNF), 29 cells (RAPA +BDNF). ***$p < 0.001$, **$p < 0.01$; *ns*, nonsignificant (Kruskal-Wallis test followed by Dunn's multiple-comparison *post hoc* test). (**D-G**) Dynamics of p150^{Glued}-Tdtomato and AP-2β-GFP co-transport in axons of neurons that were treated for 2 h with 0.1% DMSO or 100 nM rapamycin (RAPA). (**D**) Representative snapshots of 60 μm segment of axon and (**E**) corresponding kymographs of p150^{Glued}-Tdtomato- and AP-2β-GFP-positive objects. See also Supplementary Fig. S1 and Supplementary Movies S1-4. Scale bar = 10 μm. (**F**) Number of mobile p150^{Glued}-Tdtomato/AP-2β-GFP-positive objects in axons per 60 μm. The data are expressed as the mean ± SEM. N = 4 independent experiments. n = 15 cells per variant. *ns*, non significant (Mann-Whitney test). (**G**) Number of all p150^{Glued}-tdTomato/AP-2β-GFP objects in axons per 60 μm. The data are expressed as mean ± SEM. N = 4 independent experiments. n = 15 cells per variant. *$p < 0.05$ (Mann-Whitney test). (**H-K**) Dynamics of p150^{Glued}-Tdtomato and AP-2β-GFP co-transport in axons of neurons that were treated for 2 h with 0.1% DMSO and 15 min with 50 ng/ml BDNF (DMSO+BDNF) or 2 h with 100 nM rapamycin and 15 min with 50 ng/ml BDNF (RAPA+BDNF). (**H**) Representative snapshots of 60 μm segment of axon and (**I**) corresponding kymographs of p150^{Glued}-Tdtomato- and AP-2β-GFP-positive objects. See also Supplementary Fig. S1 and Supplementary Movies S5-8. Scale

bar = 10 μm. (**J**) Number of mobile p150^{Glued}-Tdtomato/AP-2β-GFP-positive objects in axons per 60 μm. The data are expressed as mean ± SEM. N = 4 independent experiments. n = 15 cells per variant. *p < 0.05 (Mann-Whitney test). **(K)** Number of all p150^{Glued}-tdTomato/AP-2β-GFP objects in axons per 60 μm. The data are expressed as mean ± SEM. N = 4 independent experiments. n = 15 cells per variant. *p < 0.05 (Mann-Whitney test).

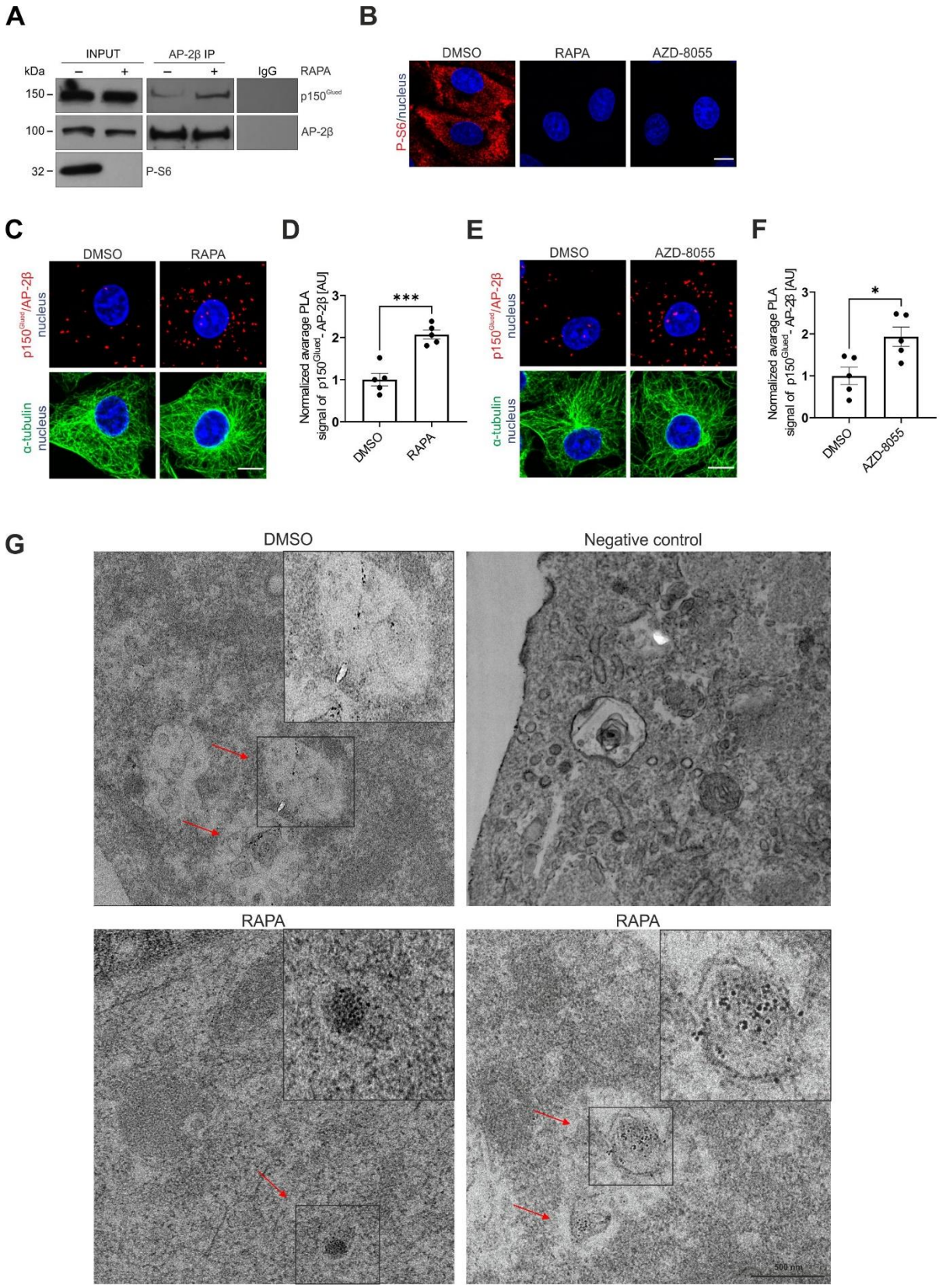

Fig. 2. mTORC1 inhibition increases p150^{Glued}–AP-2 interaction in non-neuronal cells.

(**A**) Western blot analysis of levels of endogenous p150^{Glued}, AP-2β, P-S6 (Ser235/236), and

co-immunoprecipitation of endogenous AP-2β with p150^{Glued} from HEK293T cells that were treated for 2 h with 0.1% DMSO (RAPA-) or 100 nM rapamycin (RAPA+). Input, 10% of lysate used for immunoprecipitation. Shown is a representative example from N = 5 independent experiments. (**B**) Representative images of Rat2 cells that were treated for 2 h with 0.1% DMSO (RAPA-), 100 nM rapamycin (RAPA+), or 100 nM AZD-8055 with immunofluorescently labeled endogenous P-S6 (Ser235/236) (red) and nucleus stained with Hoechst 33258 (blue). Scale bar = 10 µm. (**C**) Representative images of Rat2 fibroblasts with PLA p150^{Glued}/AP-2β signals (red), immunofluorescently labeled tubulin (green), and DAPI-stained nuclei (blue) that were treated for 2 h with 0.1% DMSO or 100 nM rapamycin (RAPA). Scale bar = 10 µm. (**D**) Quantification of the number of p150^{Glued}/AP-2β PLA puncta in cells that were treated as in C. The data are expressed as the mean number of PLA puncta per cell, normalized to the control variant (DMSO) ± SEM. N = 5 independent experiments. n = 201 cells for each experimental variant. ***p < 0.001 (Student's t-test). (**E**) Representative images of Rat2 fibroblasts with PLA p150^{Glued}/AP-2β signals (red), immunofluorescently labeled tubulin (green), and DAPI-stained nuclei (blue) that were treated for 2 h with 0.1% DMSO or 100 nM AZD-8055. Scale bar = 10 µm. (**F**) Quantification of the number of p150^{Glued}/AP-2β PLA puncta in cells that were treated as in E. The data are expressed as the mean number of PLA puncta per cell, normalized to the control variant (DMSO) ± SEM. N = 5 independent experiments. n = 211 cells (DMSO), 188 cells (AZD-8055). *p < 0.05 (Student's t-test). (**G**) Representative electron microscopy images of Rat2 fibroblasts after 2 h treatment with 0.1% DMSO or 100 nM rapamycin (RAPA) subjected to PLA for p150^{Glued}/AP-2β with and without (negative control) primary antibodies. Red arrows point to PLA signalsthat co-occurred with organelles resambling lysosomes or autophagosomes n = 30 cells per variant. N = 3 independent experiments. Scale bar = 500 nm.

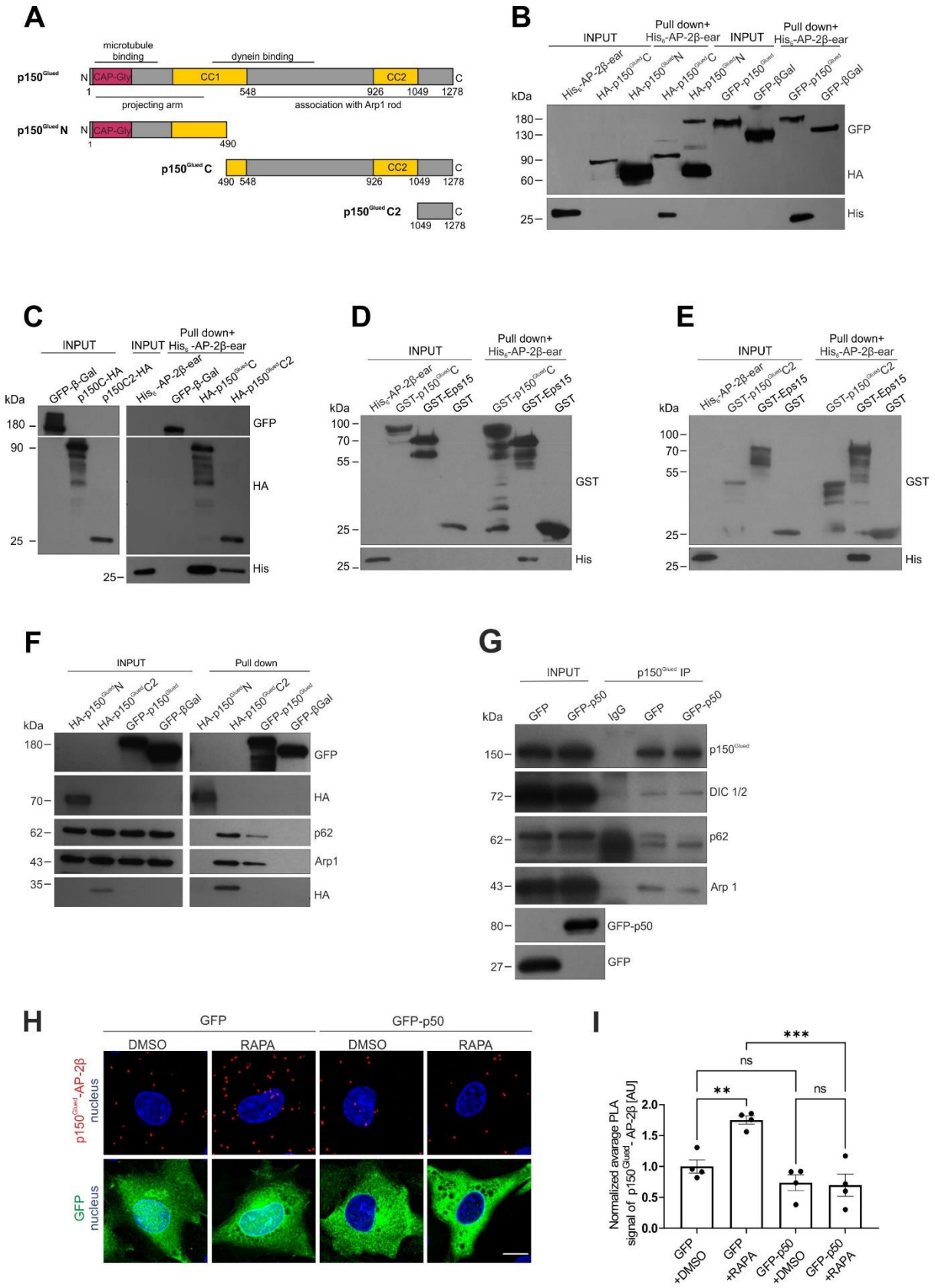

Fig. 3. AP-2β interaction with p150^{Glued} is indirect and requires intact dynactin-dynein complex. (**A**) Diagram of the full p150^{Glued} and fragments N, C and C2 used in this study. (**B**)

Western blot analysis of *E. coli*-produced His-AP-2β-ear binding to *in vivo* biotinylated AviHA-tagged p150^{Glued} N or C fragments or AviGFP-tagged p150^{Glued} or AviGFP-tagged β-galactosidase pulled down from HEK293T cells using Avi-tag pull down. Input, 10% of lysate added to the assay. Shown is a representative example from N = 3 independent experiments. (**C**) Western blot analysis of *E. coli*-produced His-AP-2β-ear binding to *in vivo* biotinylated AviHA-tagged p150^{Glued} C or C2 fragments or AviGFP-tagged p150^{Glued} or AviGFP-tagged β-galactosidase pulled down from HEK293T cells using Avi-tag pull down. Input, 10% of lysate added to the assay. Shown is a representative example from N = 2 independent experiments. (**D, E**) Western blot analysis of pull down of *E. coli*-purified recombinant GST- p150^{Glued} C, GST- p150^{Glued} C2, GST-Eps15, or GST (negative control) with recombinant His-AP-2β ear. Shown is a representative example from N = 2 independent experiments. (**F**) Western blot analysis of endogenous p62 and Arp1 binding to *in vivo* biotinylated AviHA-tagged p150^{Glued} N or C2 or full AviGFP-tagged p150^{Glued} or AviGFP-tagged β-galactosidase pulled down from HEK293T cells using Avi-tag pull down. Shown is a representative example from N = 3 independent experiments. (**G**) Western blot analysis of the co-immunoprecipitation of endogenous p150^{Glued} with other subunits of dynactin-dynein complex (DIC1/2, p62, and Arp1) from HEK293T cells that were transfected with pEGFPC1 or pEGFPC1-p50 plasmids. Shown is a representative example from N = 3 independent experiments. (**H**) Representative images of Rat2 fibroblasts that were transfected with pEGFPC1 or pEGFPC1-p50 (green), with p150^{Glued}/AP-2β PLA signals (red) and DAPI-stained nuclei (blue), and treated for 2 h with 0.1% DMSO or 100 nM rapamycin (RAPA). Scale bar = 10 μm. (**I**) Quantification of the number of p150^{Glued}/AP-2β PLA puncta in cells that were treated as in H. The data are expressed as the mean number of PLA puncta per cell, normalized to the control variant (GFP + DMSO) ± SEM. N = 4 independent experiments. n = 96 cells (GFP + DMSO), 81 cells (GFP + RAPA), 91 cells (GFP-p50 + DMSO), 92 cells (GFP-p50 + RAPA). $^{**}p < 0.01$, $^{***}p < 0.001$

(two-way ANOVA followed by Tukey's multiple-comparison *post hoc* test).

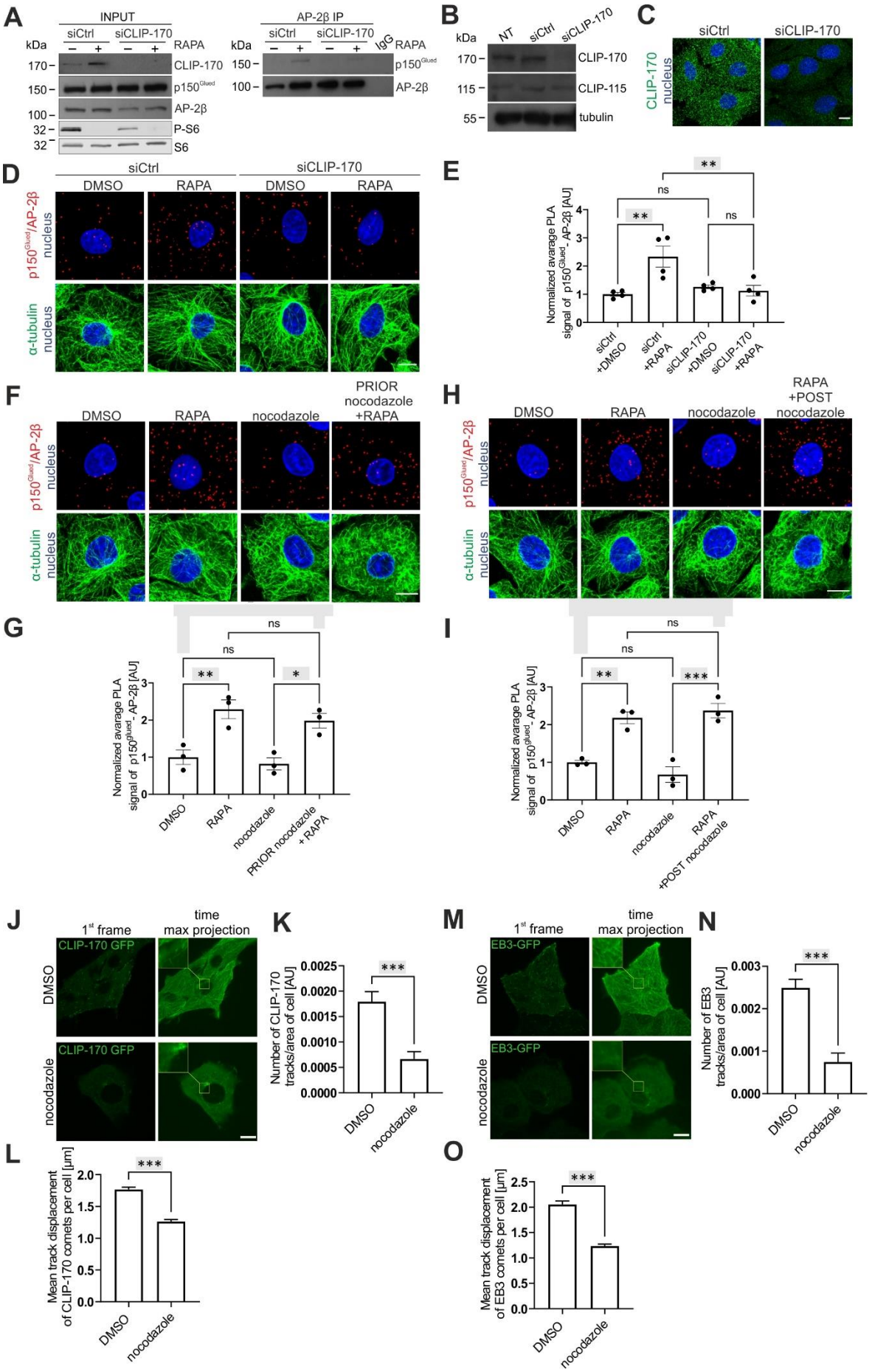
A
INPUT
siCtrl
siCLIP-170
kDa
RAPA
170
150
100
32
32
CLIP-170
p150Glued
AP-2β
P-S6
S6
AP-2β IP
IgG
B
NT
siCtrl
siCLIP-170
CLIP-170
CLIP-115
tubulin
C
siCtrl
siCLIP-170
CLIP-170
nucleus
D
DMSO
RAPA
p150Glued/AP-2β
α-tubulin
nucleus
E
Normalized avarage PLA signal of p150Glued, AP-2β [AU]
ns
**
siCtrl +DMSO
siCtrl +RAPA
siCLIP-170 +DMSO
siCLIP-170 +RAPA
F
nocodazole
PRIOR nocodazole +RAPA
G
*
DMSO
RAPA
nocodazole
PRIOR nocodazole + RAPA
H
RAPA +POST nocodazole
I
***
+POST nocodazole
J
1st frame
time max projection
CLIP-170 GFP
DMSO
nocodazole
K
Number of CLIP-170 tracks/area of cell [AU]
L
Mean track displacement of CLIP-170 comets per cell [µm]
M
EB3-GFP
N
Number of EB3 tracks/area of cell [AU]
O
Mean track displacement of EB3 comets per cell [µm]

Fig. 4. CLIP-170 but not microtubule dynamics is needed for AP-2–dynactin interaction. (**A**) Western blot analysis of endogenous CLIP-170, p150^{Glued}, AP-2β, S6, P-S6 (Ser235/236) levels and co-immunoprecipitation of endogenous AP-2β with p150^{Glued} in HEK293T cells that were transfected with control siRNA (siCtrl) or siRNA agains human CLIP-170 (siCLIP-170) and treated for 2 h with 0.1% DMSO or 100 nM rapamycin (RAPA). Input, 10% of lysate added for immunoprecipitation. Shown is a representative example from N = 3 independent experiments. (**B**) Western blot analysis of endogenous CLIP-170 and CLIP-115 levels in non-transfected Rat2 cells or Rat2 cells that were transfected with siCtrl or rat siCLIP-170. (**C**) Representative images of Rat2 cells that were transfected with siCtrl or rat siCLIP-170, with immunofluorescently labeled endogenous CLIP-170 (green) and nucleus stained with Hoechst 33258 (blue). Scale bar = 10 μm. (**D**) Representative images of Rat2 fibroblasts that were transfected with siCtrl or rat siCLIP-170, with PLA p150^{Glued}/AP-2β signals (red), immunofluorescently labeled tubulin (green), and DAPI-stained nuclei (blue), and treated for 2 h with 0.1% DMSO or 100 nM rapamycin (RAPA). Scale bar = 10 μm. (**E**) Quantification of the number of p150^{Glued}/AP-2β PLA puncta in cells that were treated as in D. The data are expressed as the mean number of PLA puncta per cell, normalized to the control variant (siCtrl + DMSO) ± SEM. N = 4 independent experiments. n = 149 cells (siCtrl + DMSO), 130 cells (siCtrl + RAPA), 161 cells (siCLIP-170 + DMSO), 142 cells (siCLIP-170 + RAPA). $^{**}p < 0.01$ (two-way ANOVA followed by Tukey's multiple-comparison *post hoc* test). (**F**) Representative images of Rat2 fibroblasts with PLA p150^{Glued}/AP-2β signals (red), immunofluorescently labeled tubulin (green), and DAPI-stained nuclei (blue) that were treated for 2 h with 0.1% DMSO or 100 nM rapamycin (RAPA) or treated for 2 h 15 min with 100 nM nocodazole alone or in combination with 100 nM rapamycin added 15 min after nocodazole (PRIOR nocodazole + RAPA). Scale bar = 10 μm. (**G**) Quantification of the number of p150^{Glued}/AP-2β PLA puncta in cells that were treated as in F. The data are expressed as the

mean number of PLA puncta per cell, normalized to the control variant (DMSO) ± SEM. *N* = 3 independent experiments. *n* = 126 cells (DMSO), 125 cells (RAPA), 133 cells (nocodazole), 139 cells (PRIOR nocodazole + RAPA). *$p < 0.05$, **$p < 0.01$ (one-way ANOVA followed by Tukey's multiple-comparison *post hoc* test). (**H**) Representative images of Rat2 fibroblasts with PLA p150^{Glued}/AP-2β signals (red), immunofluorescently labeled tubulin (green), and DAPI-stained nuclei (blue) that were treated for 2 h with 0.1% DMSO or 100 nM rapamycin (RAPA) or treated for 1 h with 100 nM nocodazole alone or added in the middle of 2 h 100 nM rapamycin incubation (RAPA + POST nocodazole). Scale bar = 10 μm. (**I**) Quantification of the number of p150^{Glued}/AP-2β PLA puncta in cells that were treated as in H. The data are expressed as the mean number of PLA puncta per cell, normalized to the control variant (DMSO) ± SEM. *N* = 3 independent experiments. *n* = 128 cells (DMSO), 118 cells (RAPA), 136 cells (nocodazole), 121 cells (RAPA + POST nocodazole). **$p < 0.01$, ***$p < 0.001$ (one-way ANOVA followed by Tukey's multiple-comparison *post hoc* test). (**J**) Representative images from time-lapse movies of microtubule dynamics in Rat2 cells, measured by microtubule plus-end tracking behavior of CLIP-170-GFP after 1 h treatment with 0.1% DMSO or 100 nM nocodazole. Images in the left column show the first frame from the time-lapse movies. Images in the right column show maximum intensity projections from Z-stacks of all 600 frames. Scale bar = 10 μm. See Movies 9 and 10. (**K**) Quantification of the number of all microtubule tracks per cell divided by cell area for CLIP-170-GFP. The data are expressed as mean ± SEM. *N* = 3 independent experiments. *n* = 31 cells (DMSO), 25 cells (nocodazole). ***$p < 0.001$ (Mann-Whitney test). (**L**) Quantification of the mean track run length of CLIP-170-GFP comets per cell. The data are expressed as mean ± SEM. *N* = 3 independent experiments. *n* = 31 cells (DMSO), 25 cells (nocodazole). ***$p < 0.001$ (Mann-Whitney test). (**M**) Representative images from time-lapse movies of microtubule dynamics in Rat2 cells, measured by microtubule plus-end tracking behavior of EB3-GFP after 1 h

treatment with 0.1% DMSO or 100 nM nocodazole. Images in the left column show the first frame from the time-lapse movies. Images in the right column show maximum intensity projections from Z-stacks of all 600 frames. Scale bar = 10 μm. See Movies 11 and 12. (**N**) Quantification of the number of all microtubule tracks per cell divided by cell area for EB3-GFP. The data are expressed as mean ± SEM. N = 3 independent experiments. n = 23 cells (DMSO), 24 cells (nocodazole). ***$p < 0.001$ (Mann-Whitney test). (**O**) Quantification of the mean track run lengths of EB3-GFP comets per cell. The data are expressed as mean ± SEM. N = 3 independent experiments. n = 23 cells (DMSO), 24 cells (nocodazole). ***$p < 0.001$ (Mann-Whitney test).

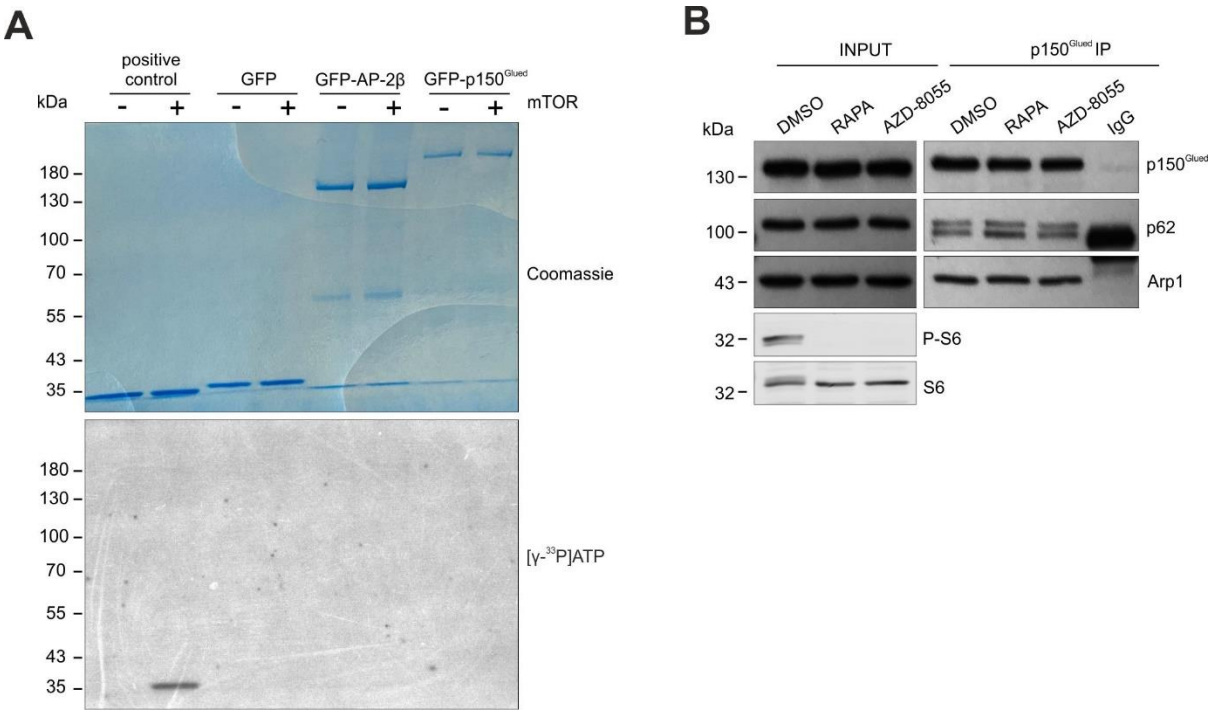

Fig. 5. mTOR does not phosphorylate AP-2β or p150^{Glued} and does not affect p150^{Glued} binding to Arp1 or p62. (**A**) Results of kinase assay using recombinant active mTOR fragment and GFP-AP-2β, GFP-p150^{Glued}, or EGFPC1 (negative control) immunoprecipitated from HEK293T cells as substrates. Commercial mTOR substrate served as a positive control. The upper panel shows Coomassie staining of SDS-PAGE gels with the analyzed proteins. The lower panel shows the radioactive signal level of [γ-33P] ATP incorporated into the analyzed

proteins. Shown is a representative example from *N* = 2 independent experiments. (**B**) Western blot analysis of endogenous p150^{Glued}, Arp1, p62, S6, P-S6 (Ser235/236) levels in HEK293T cells and co-immunoprecipitation of p150^{Glued}, Arp1, and p62 from HEK293T cells that were treated for 2 h with 0.1% DMSO, 100 nM rapamycin (RAPA), or 100 nM AZD 80550. Shown is a representative example from *N* = 2 independent experiments.

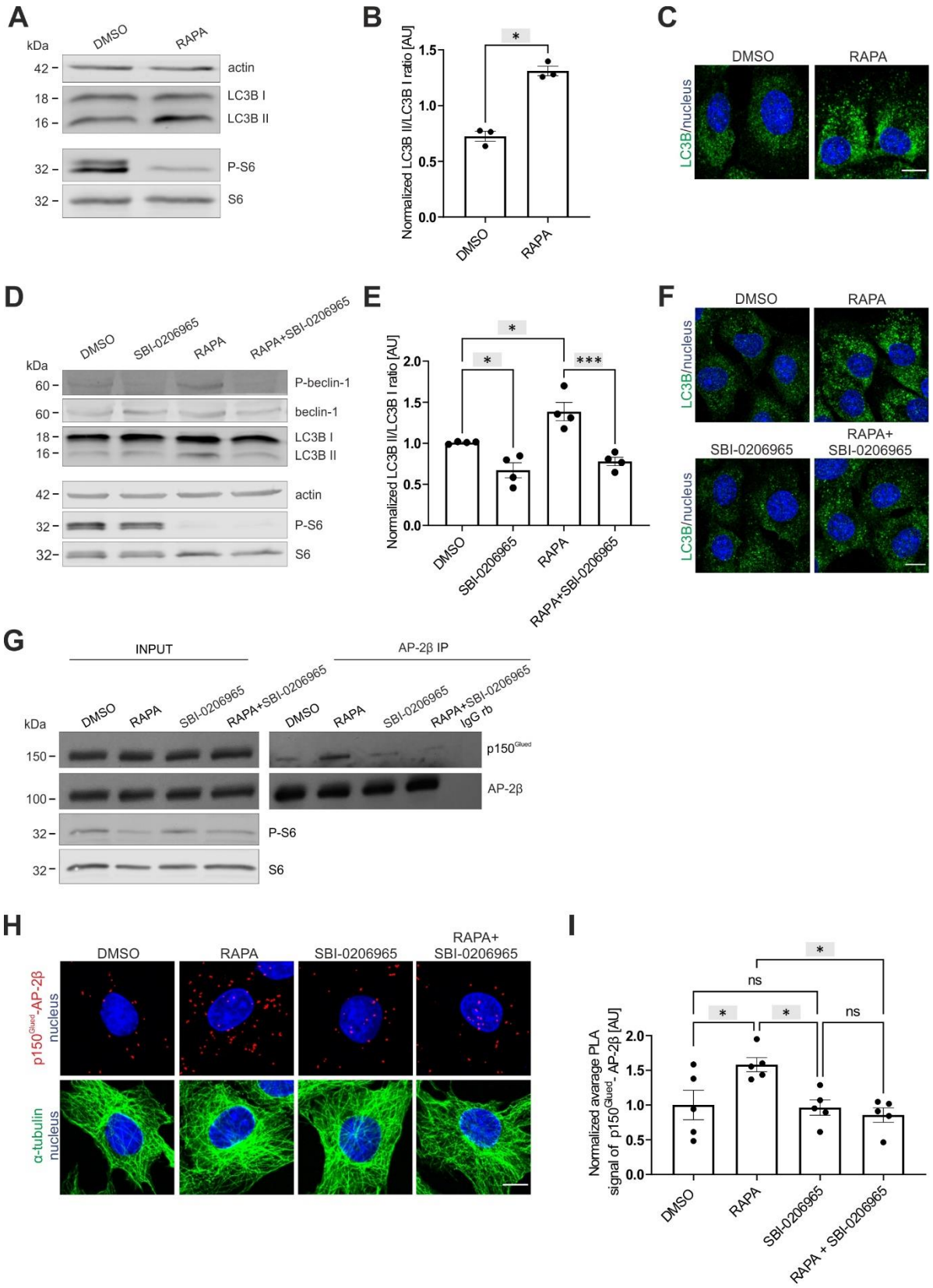

Fig. 6. Autophagy induction upon mTORC1 inhibition is needed for AP-2–dynactin interaction. (A) Western blot analysis of endogenous actin, LC3B I, LC3B II, P-S6

(Ser235/236) and S6 levels in Rat2 fibroblasts that were treated for 2 h with 0.1% DMSO or 100 nM rapamycin (RAPA). Shown is a representative example from N = 3 independent experiments. (**B**) Densitometry analysis of normalized LC3B II/LCB I ratio in Rat2 cells that were treated as in A ± SEM. N = 3 independent experiments. *$p \leq 0.05$ (one-tailed Mann Whitney test). (**C**) Representative images of Rat2 cells that were treated for 2 h with 0.1% DMSO or 100 nM rapamycin (RAPA) with immunofluorescently labeled endogenous LC3B (green) and nucleus stained with Hoechst 33258 (blue). Scale bar = 10 μm. (**D**) Western blot analysis of endogenous P-beclin-1 (Ser30), beclin-1, LC3B I, LC3BII, actin, P-S6 (Ser235/236) and S6 levels in Rat2 fibroblasts treated with 0.1% DMSO for 2 h, 100 nM rapamycin (RAPA) for 2 h, 25 μM SBI-0206965 for 2 h 30 min, or 25 μM SBI-0206965 for 30 min and 100 nM rapamycin for 2 h (RAPA + SBI-0206965). (**E**) Densitometry analysis of normalized LC3B II/LCB I ratio in Rat2 cells that were treated as in D ± SEM. N = 4 independent experiments. *$p < 0.05$, ***$p < 0.001$ (one-way ANOVA followed by Tukey's multiple-comparison *post hoc* test). (**F**) Representative images of Rat2 cells that were treated with 0.1% DMSO for 2 h, 100 nM rapamycin (RAPA) for 2 h, 25 μM SBI-0206965 for 2 h 30 min, or 25 μM SBI-0206965 for 30 min and 100 nM rapamycin for 2 h (RAPA + SBI-0206965), with immunofluorescently labeled endogenous LC3B (green) and nucleus stained with Hoechst 33258 (blue). Scale bar = 10 μm. (**G**) Western blot analysis of endogenous $p150^{Glued}$, AP-2β, S6, P-S6 (Ser235/236) and co-immunoprecipitation of endogenous AP-2β with $p150^{Glued}$ in HEK293T cells that were treated with 0.1% DMSO for 2 h, 100 nM rapamycin (RAPA) for 2 h, 25 μM SBI-0206965 for 2 h 30 min, or 25 μM SBI-0206965 for 30 min and 100 nM rapamycin for 2 h (RAPA + SBI-0206965). Input, 10% of lysate used for immunoprecipitation. Shown is a representative example from N = 2 independent experiments. (**H**) Representative images of Rat2 fibroblasts with PLA $p150^{Glued}$/AP-2β signals (red), immunofluorescently labeled tubulin (green), and DAPI-stained nuclei (blue) that were treated

with 0.1% DMSO for 2 h, 100 nM rapamycin (RAPA) for 2 h, 25 μM SBI-0206965 for 2 h 30 min, or 25 μM SBI-0206965 for 30 min and 100 nM rapamycin for 2 h (RAPA + SBI-0206965). Scale bar = 10 μm. (**I**) Quantification of the number of $p150^{Glued}$/AP-2β PLA puncta in cells that were treated as in H. The data are expressed as the mean number of PLA puncta per cell, normalized to the control variant (DMSO) ± SEM. $N = 5$ independent experiments, $n = 184$ cells (DMSO), 189 cells (RAPA), 169 cells (SBI-0206965), 174 cells (RAPA + SBI-0206965). $^{*}p < 0.05$ (one-way ANOVA followed by Tukey's multiple-comparison *post hoc* test).

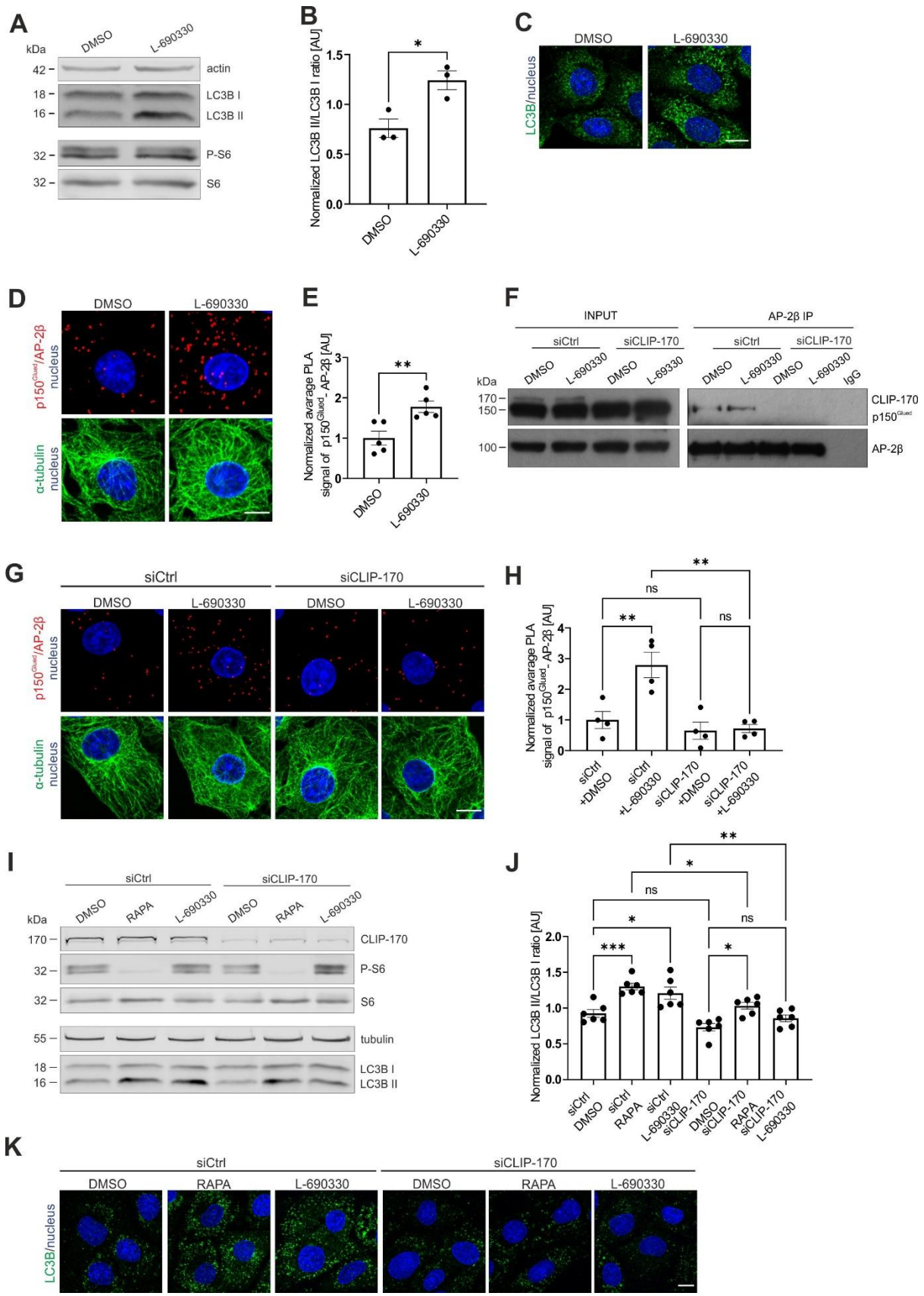

Fig. 7. AP-2–dynactin interaction is induced by autophagy even when mTOR activity is preserved. (**A**) Western blot analysis of endogenous actin, LC3B I, LC3B II, P-S6

(Ser235/236) and S6 levels in Rat2 fibroblasts that were treated for 3 h with 0.1% DMSO or 100 μM L-690330. Shown is a representative example from N = 3 independent experiments. (**B**) Densitometry analysis of normalized LC3B II/LCB I ratio in Rat2 cells that were treated as in A ± SEM. N = 3 independent experiments. *$p \leq 0.05$, (one-tailed Mann Whitney test). (**C**) Representative images of Rat2 cells that were treated for 3 h with 0.1% DMSO or 100 μM L-690330 with immunofluorescently labeled endogenous LC3B (green) and nuclei stained with Hoechst 33258 (blue). Scale bar = 10 μm. (**D**) Representative images of Rat2 fibroblasts with PLA $p150^{Glued}$/AP-2β signals (red), immunofluorescently labeled tubulin (green), and DAPI-stained nuclei (blue) that were treated for 3 h with 0.1% DMSO or 100 μM L-690330. Scale bars =10 μm. (**E**) Quantification of the number of $p150^{Glued}$/AP-2β PLA puncta in cells that were treated as in D. The data are expressed as the mean number of PLA puncta per cell, normalized to the control variant (DMSO) ± SEM. N = 5 independent experiments. n = 200 cells (DMSO), 181 cells (L-690330). **$p < 0.01$ (Student's t-test). (**F**) Western blot analysis of endogenous CLIP-170, $p150^{Glued}$ and AP-2β levels and co-immunoprecipitation of endogenous AP-2β with $p150^{Glued}$ in HEK293T cells that were transfected with control siRNA (siCtrl) or siRNA agains human CLIP-170 (siCLIP-170) and treated for 3 h with 0.1% DMSO or 100 μM L-69330. Input, 10% of lysate used for immunoprecipitation. Shown is a representative example from N = 2 independent experiments. (**G**) Representative images of Rat2 fibroblasts that were transfected with siCtrl or rat siCLIP-170 with PLA $p150^{Glued}$/AP-2β signals (red), immunofluorescently labeled tubulin (green), and DAPI-stained nuclei (blue) and treated for 3 h with 0.1% DMSO or 100 μM L-690330. Scale bar = 10 μm. (**H**) Quantification of the number of $p150^{Glued}$/AP-2β PLA puncta in cells that were treated as in G. The data are expressed as the mean number of PLA puncta per cell, normalized to the control variant (siCtrl +DMSO) ± SEM. N = 4 independent experiments. n = 167 cells (siCtrl + DMSO), 163 cells (siCtrl + L-690330), 146 cells (siCLIP-170 + DMSO), 164 cells (siCLIP-170 + L-690330). **p

< 0.01 (two-way ANOVA followed by Tukey's multiple-comparison *post hoc* test). (**I**) Western blot analysis of endogenous CLIP-170, P-S6 (Ser235/236), S6, tubulin, LC3B I, and LC3B II levels in Rat-2 fibroblasts that were transfected with siCtrl or rat siCLIP-170 and treated for 2 h with 0.1% DMSO, 100 nM rapamycin (RAPA), or treated for 3 h with 100 μM L-690330. Shown is a representative example from N = 6 independent experiments. (**J**) Densitometry analysis of normalized LC3B II/LCB I ratio in Rat-2 cells that were treated as in I ± SEM. N = 6 independent experiments. *p < 0.05, **p < 0.01, ***p < 0.001 (two-way ANOVA followed by Tukey's multiple-comparison *post hoc* test). (**K**) Representative images of Rat2 cells that were transfected with siCtrl or rat siCLIP-170 and treated for 2 h with 0.1% DMSO, 100 nM rapamycin (RAPA), or treated for 3 h with 100 μM L-690330 with immunofluorescently labeled endogenous LC3B (green) and nuclei stained with Hoechst 33258 (blue). Scale bar = 10 μm.

Supplementary Figures

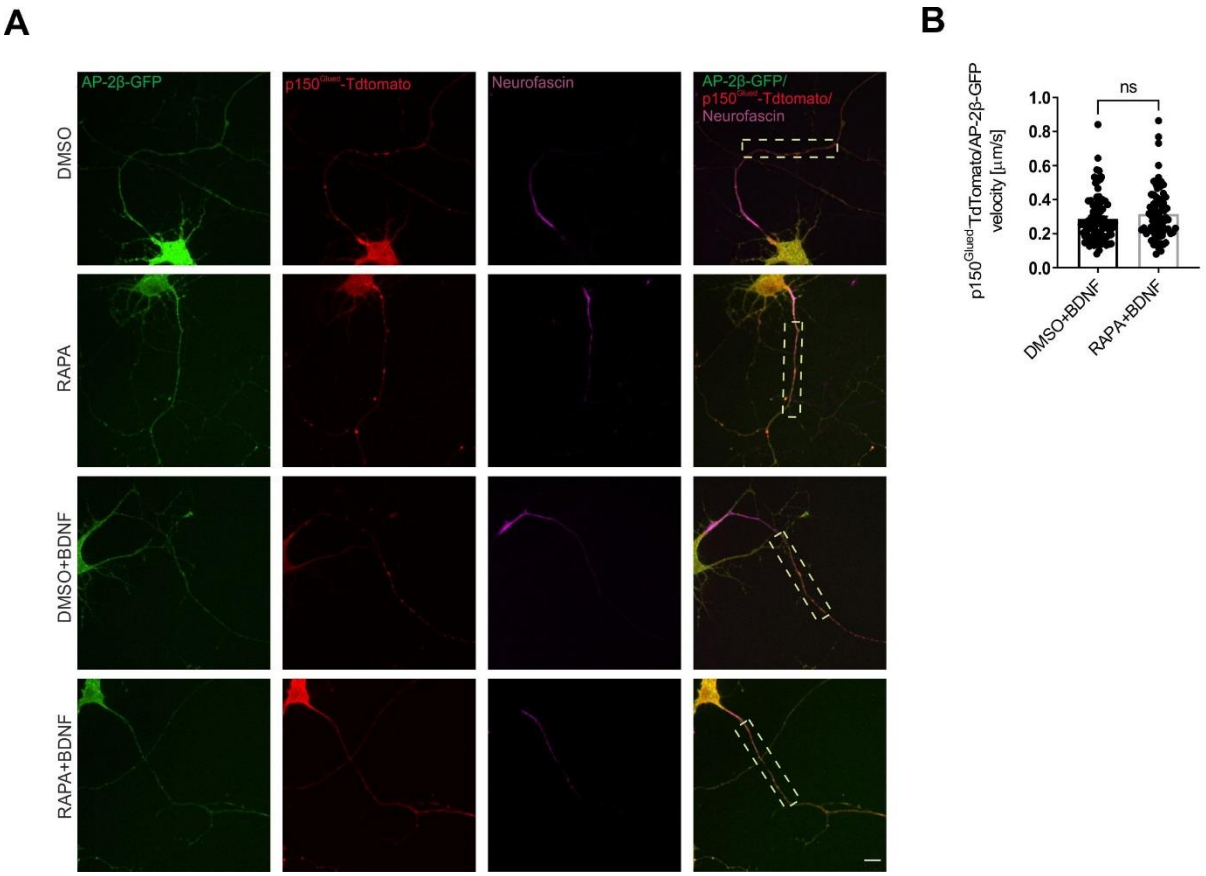

Supplementary Fig. 1. mTORC1 inhibition in neurons increases p150^{Glued}–AP-2 interaction and transport along axonal microtubules. (**A**) Snapshots of DIV7 neurons that were treated as indicated expressing p150^{Glued}-Tdtomato (red), AP-2β-GFP (green) and stained for the axon initial segment with CF640R-conjugated neurofascin antibody (magenta). Scale bar = 10 µm. (**B**) Mean velocities of p150^{Glued}-Tdtomato-AP/2β-GFP-positive objects in axons of neurons that were treated with 0.1% DMSO and 50 ng/ml BDNF (DMSO+BDNF) or 100 nM rapamycin and 50 ng/ml BDNF (RAPA+BDNF). Each point on the graph represents the speed of one object. The data are expressed as mean ± SEM. N = 4 independent experiments. n = 15 cells per variant. *ns*, nonsignificant (Mann-Whitney test).

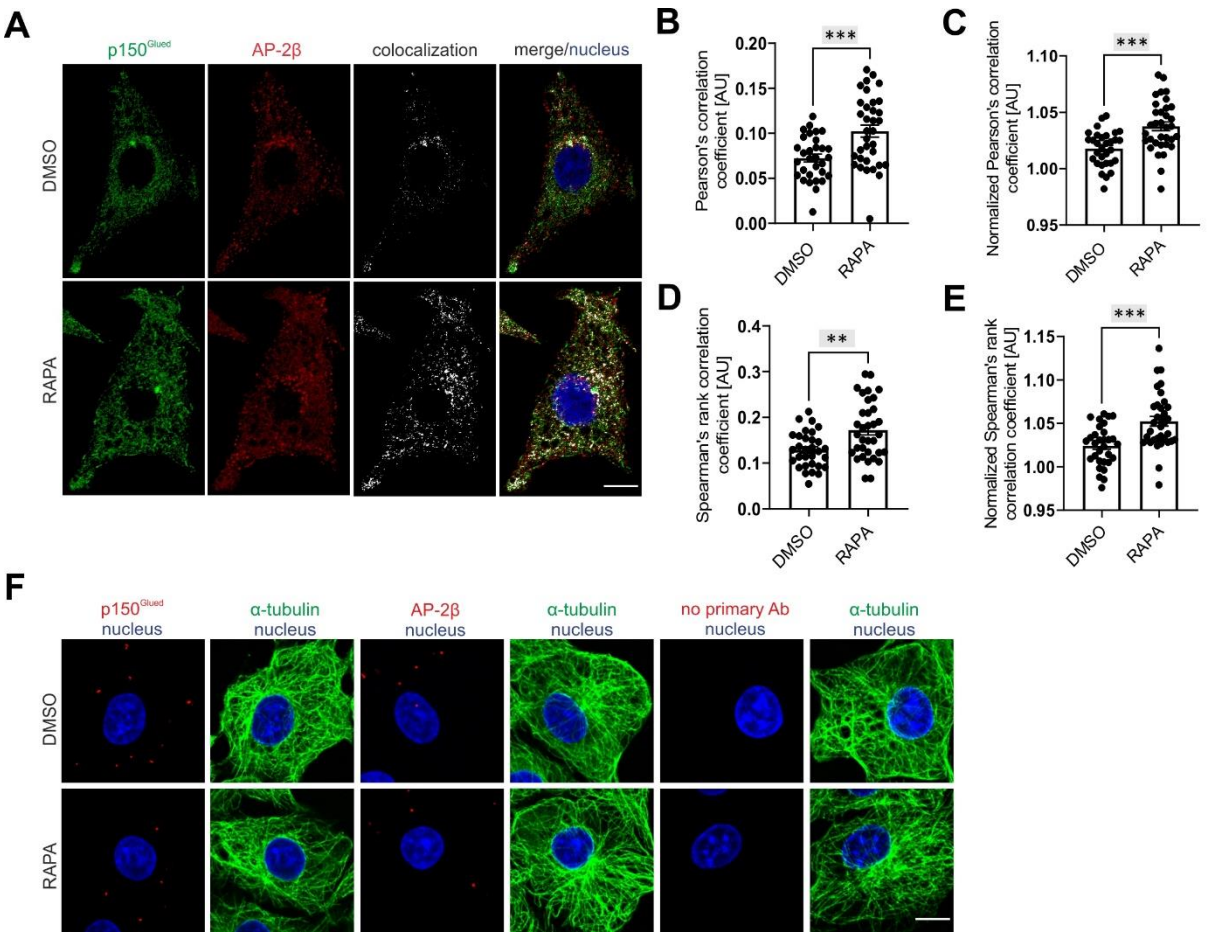

Supplementary Fig. S2. mTORC1 inhibition increases p150^{Glued}–AP-2 interaction in non-neuronal cells. (**A**) Representative images of Rat2 cells that were treated for 2 h with 0.1% DMSO or 100 nM rapamycin (RAPA) with immunofluorescently labeled endogenous p150^{Glued} (green) and AP-2β (red), additionally stained with DAPI (blue). Scale bar = 10 µm. White channel indicates p150^{Glued} and AP-2β immunofluorescent signal colocalization. (**B**) Analysis of Pearson correlation coefficients of endogenous AP-2β/p150^{Glued} colocalization without normalization. The data are expressed as the mean coefficient of co-localization of two proteins ± SEM. N = 2 independent experiments. n = 31 cells (DMSO), 34 cells (RAPA). ***p < 0.001 (Student's t-test). (**C**) Analysis of Pearson correlation coefficients of AP-2β/p150^{Glued} with normalization to the appropriate value that resulted from the random distribution of fluorescence in the cell. The data are expressed as the mean coefficient of co-localization of two proteins ± SEM. N = 2 independent experiments. n = 31 cells (DMSO), 34 cells (RAPA).

***$p < 0.001$ (Student's *t*-test). (**D**) Analysis of Spearman's rank correlation coefficient of AP-2β/p150^{Glued} colocalization without normalization. The data are expressed as the mean coefficient of co-localization of two proteins ± SEM. $N = 2$ independent experiments. $n = 31$ cells (DMSO), 34 cells (RAPA). **$p < 0.005$ (Student's *t*-test). (**E**) Analysis of Spearman's rank correlation coefficient of AP-2β/p150^{Glued} colocalization with normalization to the appropriate value that resulted from the random distribution of fluorescence in the cell. The data are expressed as the mean coefficient of co-localization of two proteins ± SEM. $N = 2$ independent experiments. $n = 31$ cells (DMSO), 34 cells (RAPA). ***$p < 0.001$ (Student's *t*-test). (**F**) Representative images of Rat2 fibroblasts with negative controls for PLA with one primary antibody present (p150^{Glued} or AP-2β) or without primary antibodies (Ab) (red), immunofluorescently labeled tubulin (green), and DAPI-stained nuclei (blue) that were treated for 2 h with 0.1% DMSO or 100 nM rapamycin (RAPA). Scale bar =10 μm.

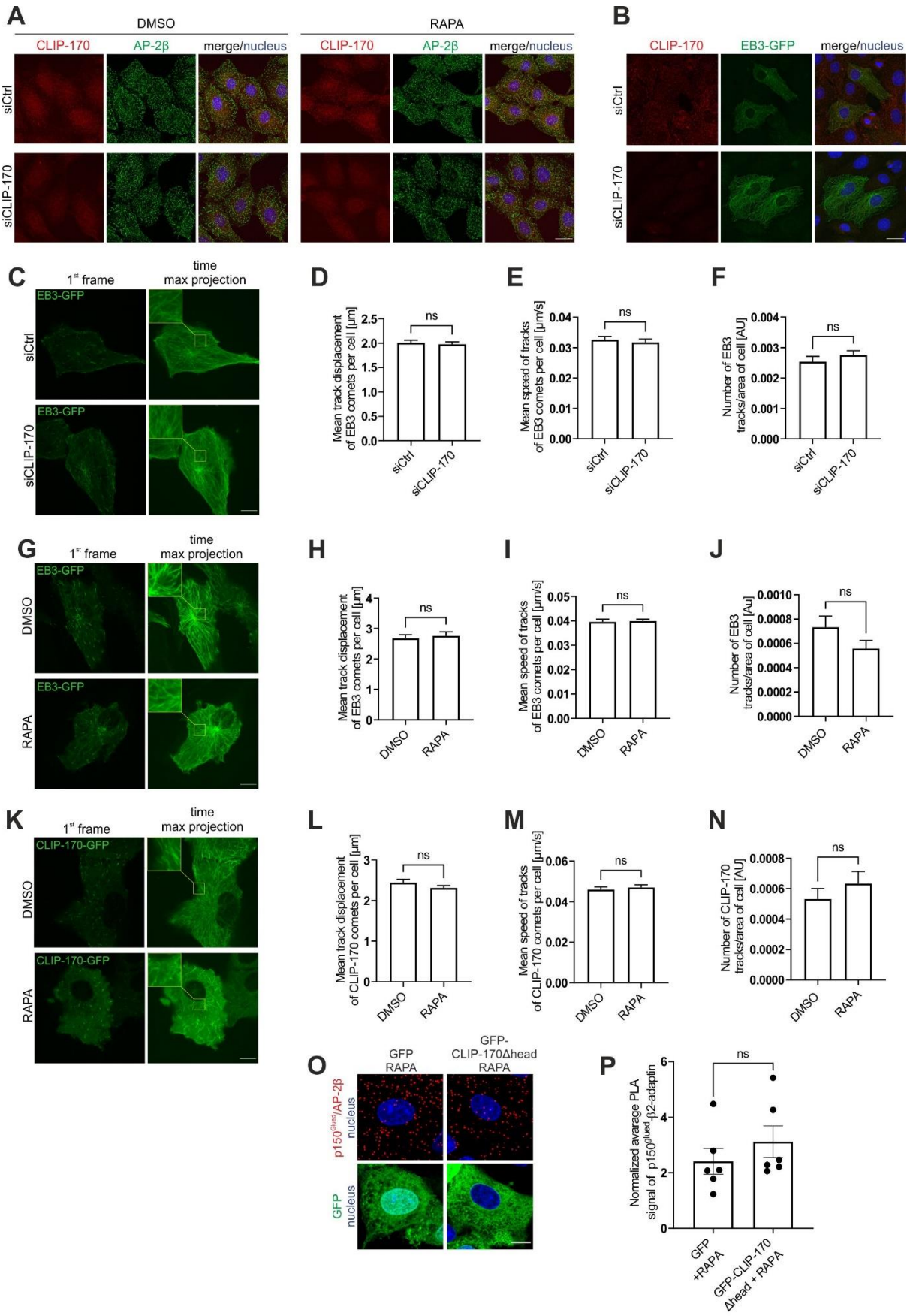

Supplementary Fig. S3. mTORC1 inhibition does not influence dynamic microtubules

and AP-2β distribution. (**A**) Representative images of fluorescently labeled endogenous CLIP-170 (red), AP-2β (green), and nucleus stained with Hoechst 33258 (blue) in Rat2 cells transfected with siCtrl or rat siCLIP-170 for 72 hours followed by treatment with 0.1 % DMSO or 100 nM rapamycin for 2 h. Scale bar = 20 μm. (**B**) Representative images of fluorescently labeled endogenous CLIP-170 (green) and nucleus stained with Hoechst 33258 (blue) in Rat2 cells transfected with siCtrl or rat siCLIP-170 and 24 h later electroporated with a plasmid encoding EB3-GFP. Cells were fixed 48 h after electroporation. Scale bars = 20 μm. (**C**) Representative images from time-lapse movies of microtubule dynamics in Rat2 cells that were transfected with siCtrl or siCLIP-170 and 24 h later electroporated with a plasmid that encoded EB3-GFP. The experiment was performed 48 h after electroporation. Images in the left column show the first frame from the time-lapse movies. Images in the right column show maximum intensity projections from Z-stacks of all 600 frames. Scale bar = 10 μm. (**D**) Quantification of the mean track run lengths of EB3-GFP comets per cell. The data are expressed as mean ± SEM. N = 3 independent experiments. n = 26 cells (siCtrl), 26 cells (siCLIP-170). *ns*, nonsignificant (Student's *t*-test). (**E**) Quantification of the mean speed of EB3-GFP comet. The data are expressed as mean ± SEM. N = 3 independent experiments. n = 26 cells (siCtrl), 26 cells (siCLIP-170). *ns*, nonsignificant (Mann-Whitney test). (**F**) Quantification of the number of all microtubule tracks per cell divided by cell area for EB3-GFP. The data are expressed as mean ± SEM. N = 3 independent experiments. n = 26 cells (siCtrl), n = 26 cells (siCLIP-170). *ns*, nonsignificant (Student's *t*-test). (**G**) Representative images from time-lapse movies of microtubule dynamics in Rat2 cells, measured by microtubule plus-end tracking behavior of EB3-GFP after 2 h treatment with 0.1% DMSO or 100 nM rapamycin (RAPA). Images in the left column show the first frame from the time-lapse movies. Images in the right column show maximum intensity projections from Z-stacks of all 600 frames. Scale bar = 10 μm. (**H**) Quantification of the mean track run lengths of EB3-GFP comets per cell. The data are

expressed as mean ± SEM. *N* = 3 independent experiments. *n* = 27 cells (DMSO), 27 cells (RAPA). *ns*, nonsignificant (Mann-Whitney test). (**I**) Quantification of the mean speed of EB3-GFP comet. The data are expressed as mean ± SEM. *N* = 3 independent experiments. *n* = 27 cells (DMSO), 27 cells (RAPA). *ns*, nonsignificant (Mann-Whitney test). (**J**) Quantification of the number of all microtubule tracks per cell divided by cell area for EB3-GFP. The data are expressed as mean ± SEM. *N* = 3 independent experiments. *n* = 27 cells (DMSO), 27 cells (RAPA). *ns*, nonsignificant (Mann-Whitney test). **(K**) Representative images from time-lapse movies of microtubule dynamics in Rat2 cells, measured by microtubule plus-end tracking behavior of CLIP-170-GFP after 2 h treatment with 0.1% DMSO or 100 nM rapamycin (RAPA). Images in the left column show the first frame from the time-lapse movies. Images in the right column show maximum intensity projections from Z-stacks of all 600 frames. Scale bar = 10 μm. (**L**) Quantification of the mean track run lengths of CLIP-170-GFP comets per cell. The data are expressed as mean ± SEM. *N* = 3 independent experiments. *n* = 35 cells (DMSO), 34 cells (RAPA). *ns*, nonsignificant (Mann-Whitney test). (**M**) Quantification of the mean speed of CLIP-170-GFP comet. The data are expressed as mean ± SEM. *N* = 3 independent experiments. *n* = 35 cells (DMSO), 34 cells (RAPA). *ns*, nonsignificant (Mann-Whitney test). (**N**) Quantification of the number of all microtubule tracks per cell divided by cell area for CLIP-170-GFP. The data are expressed as mean ± SEM. *N* = 3 independent experiments. *n* = 35 cells (DMSO), 34 cells (RAPA). *ns*, nonsignificant (Mann-Whitney test). (**O**) Representative images of Rat2 fibroblasts that were transfected with pEGFPC1 or pEGFPC1-CLIP-170Δhead (green), with PLA $p150^{Glued}$/AP-2β signals (red) and DAPI-stained nuclei (blue) and treated for 2 h with 100 nM rapamycin (RAPA). Scale bar = 10 μm. (**P**) Quantification of the number of $p150^{Glued}$/AP-2β PLA puncta in cells that were treated as in I. The data are expressed as the mean number of PLA puncta per cell, normalized to the control variant (GFP + DMSO, not shown) ± SEM. *N* = 6 independent experiments. *n* = 94 cells (GFP

+ RAPA), n = 114 cells (GFP-CLIP-170Δhead + RAPA). *ns*, non significant (Mann-Whitney test).

1A

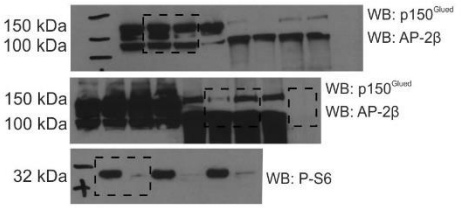

2A

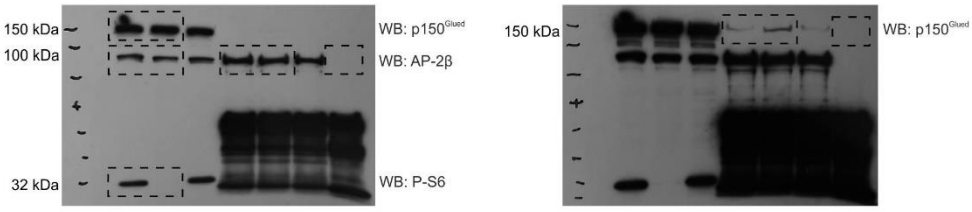

3B

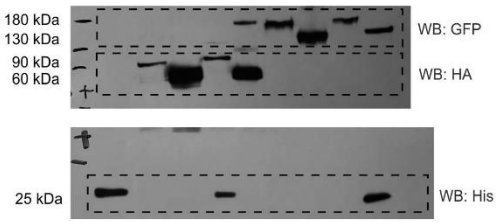

3C

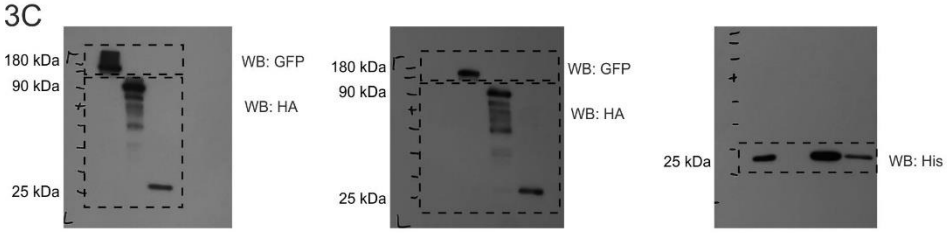

3D

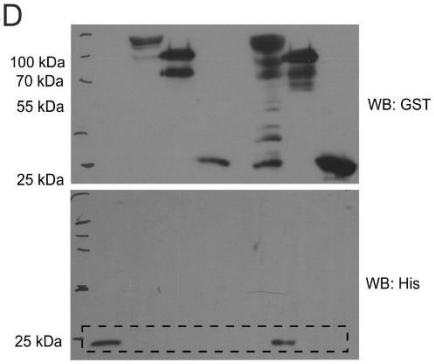

3E

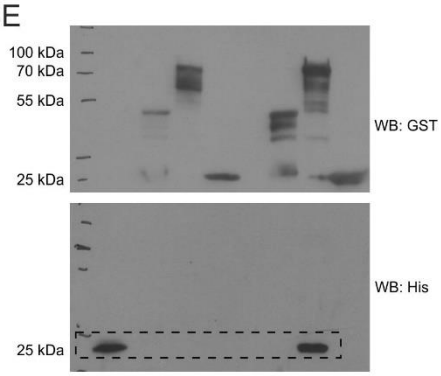

3F

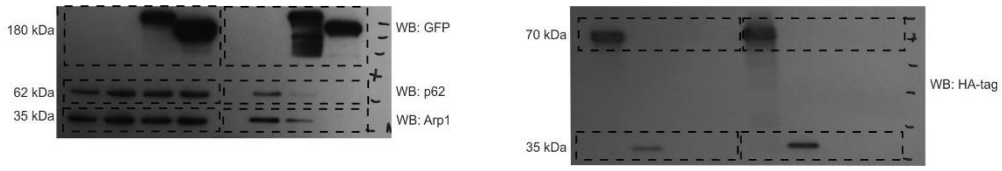

3G

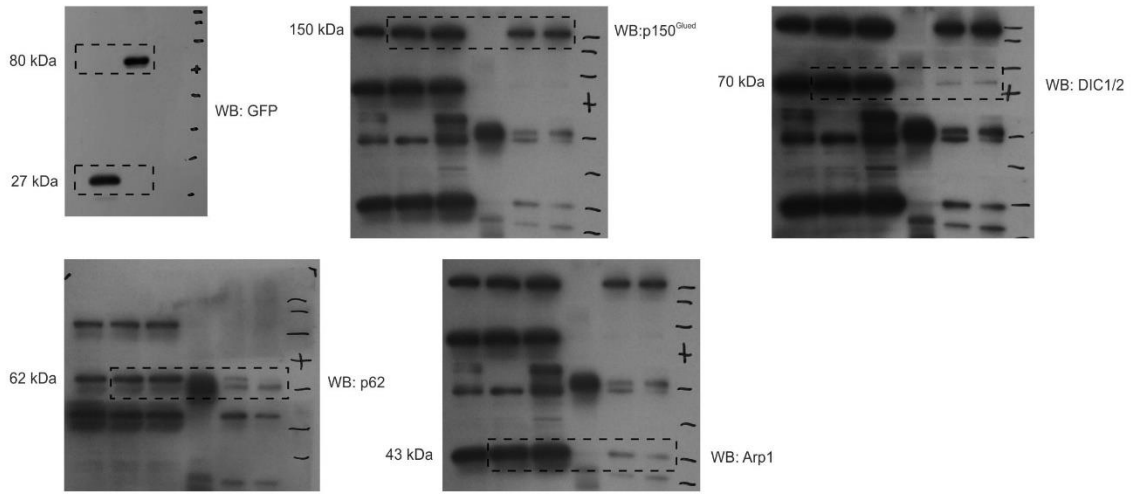
80 kDa
27 kDa
WB: GFP
150 kDa
WB:p150Glued
70 kDa
WB: DIC1/2
62 kDa
WB: p62
43 kDa
WB: Arp1

4A

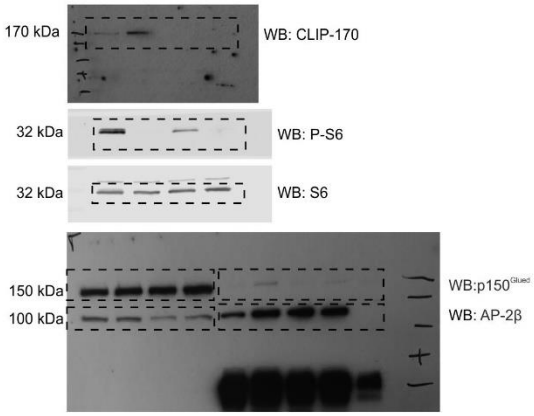
170 kDa
WB: CLIP-170
32 kDa
WB: P-S6
32 kDa
WB: S6
150 kDa
WB:p150Glued
100 kDa
WB: AP-2β

4B

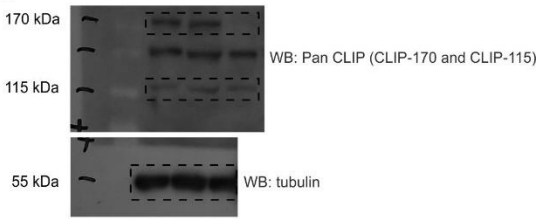
170 kDa
WB: Pan CLIP (CLIP-170 and CLIP-115)
115 kDa
55 kDa
WB: tubulin

5A

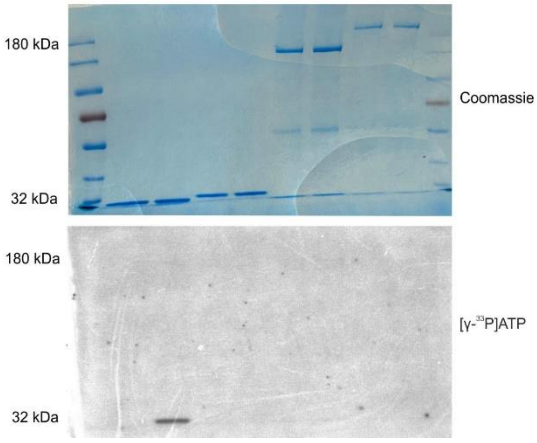
180 kDa
Coomassie
32 kDa
180 kDa
[γ-33P]ATP
32 kDa

5B

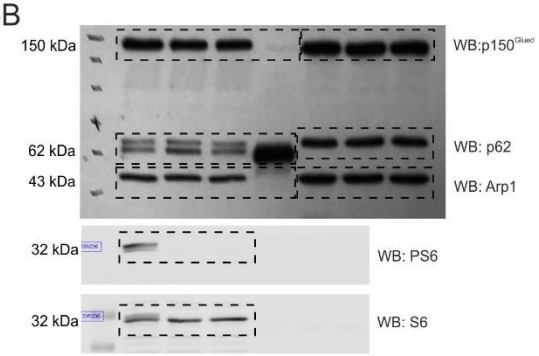
150 kDa
WB:p150Glued
62 kDa
WB: p62
43 kDa
WB: Arp1
32 kDa
WB: PS6
32 kDa
WB: S6

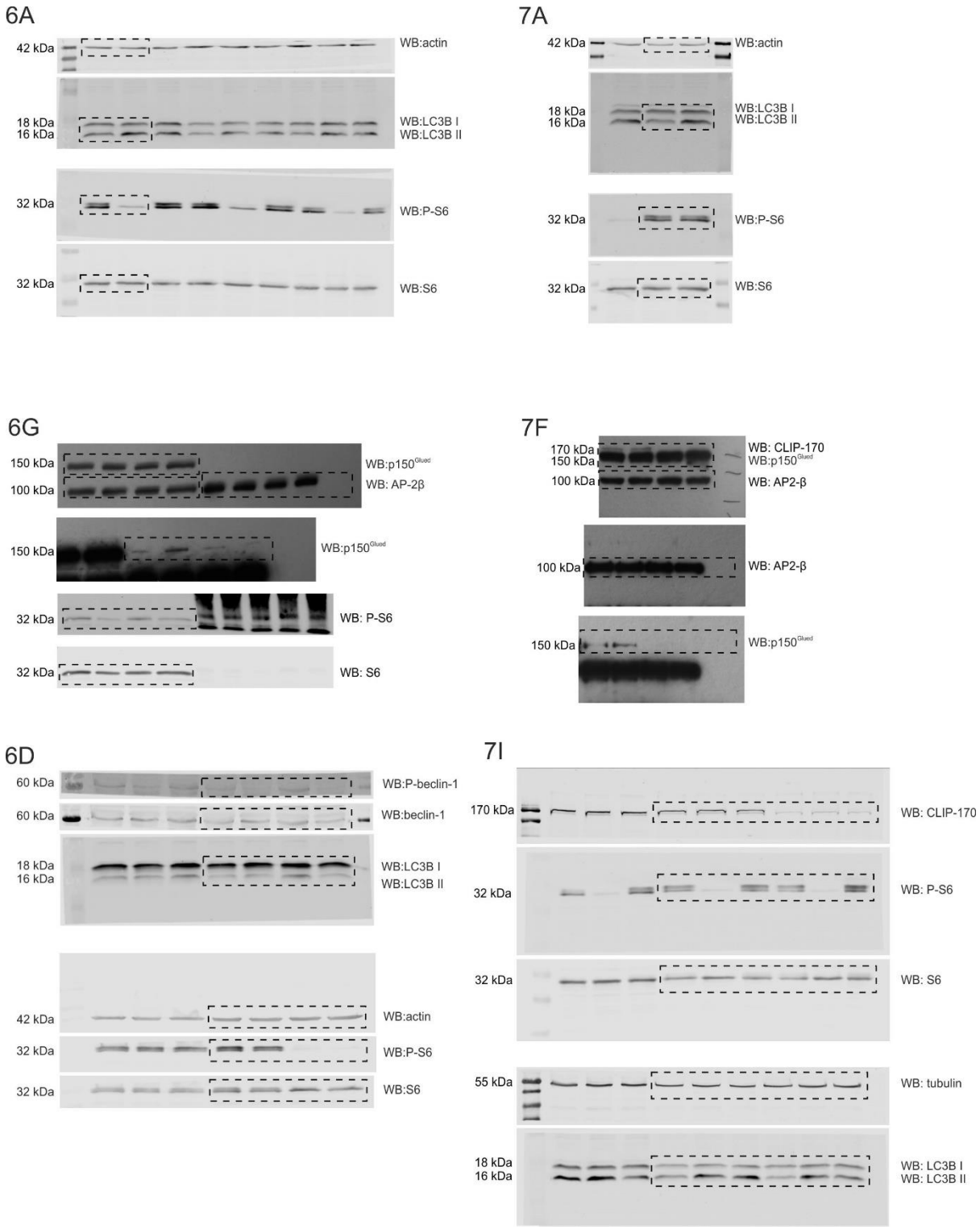

Supplementary Fig. S4. Blot transparency. Full-size blots that correspond to cropped images that are presented in the manuscript.

Movies

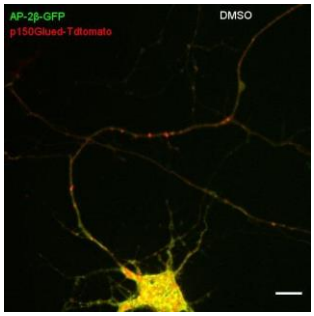

Movie 1. Hippocampal neuron that was transfected with plasmids that encoded p150^{Glued}-Tdtomato (red) and AP-2β-GFP (green) and treated for 2 h with 0.1% DMSO. Speed = 12x real time. Scale bar = 10 μm.

Movie 2. Straightened fragment of axon of neuron from Movie 1. Speed = 12x real time. Scale bar = 10 μm.

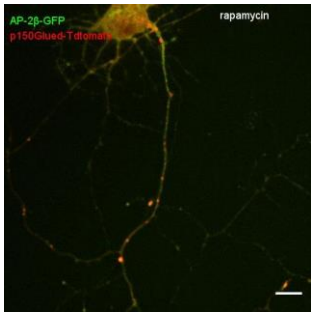

Movie 3. Hippocampal neuron that was transfected with plasmids that encoded p150^{Glued}-Tdtomato and AP-2β-GFP and treated for 2 h with 100 nM rapamycin. Speed = 12x real time. Scale bar = 10 μm.

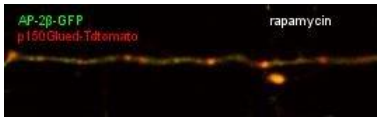

Movie 4. Straightened fragment of axon of neuron from Movie 3. Speed = 12x real time. Scale

bar = 10 μm.

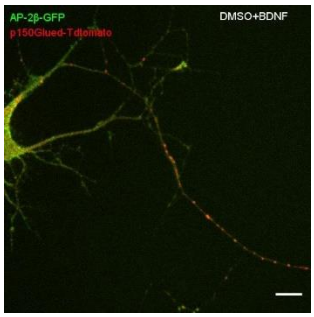

Movie 5. Hippocampal neuron that was transfected with plasmids that encoded p150^{Glued}-Tdtomato and AP-2β-GFP and treated for 2 h with 0.1% DMSO and for 15 min with 50 ng/ml BDNF. Speed = 12x real time. Scale bar = 10 μm.

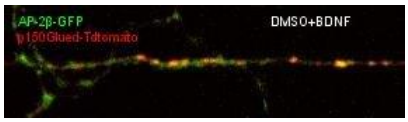

Movie 6. Straightened fragment of axon of neuron from Movie 5. Speed = 12x real time. Scale bar = 10 μm.

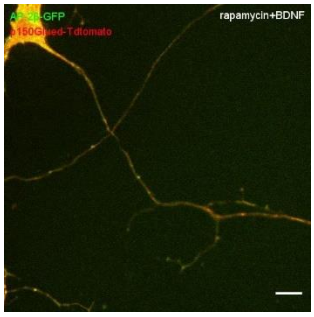

Movie 7. Hippocampal neuron that was transfected with plasmids that encoded p150^{Glued}-Tdtomato and AP-2β-GFP and treated for 2 h with 100 nM rapamycin and for 15 min with 50 ng/ml BDNF. Speed = 12x real time. Scale bar = 10 μm.

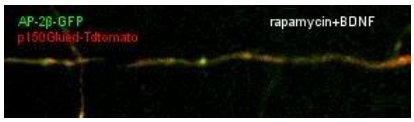

Movie 8. Straightened fragment of axon of neuron from Movie 7. Speed = 12x real time. Scale bar = 10 μm.

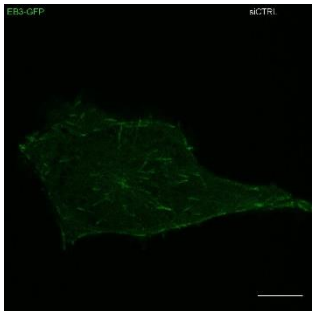

Movie 9. Rat2 cells that were transfected with siCtrl and 24 h later electroporated with a plasmid that encoded EB3-GFP. Speed = 10x real time. Scale bar = 10 μm.

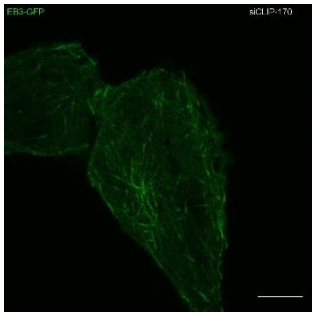

Movie 10. Rat2 cells that were transfected with siCLIP-170 and 24 h later electroporated with a plasmid that encoded EB3-GFP. Speed = 10x real time. Scale bar = 10 μm.

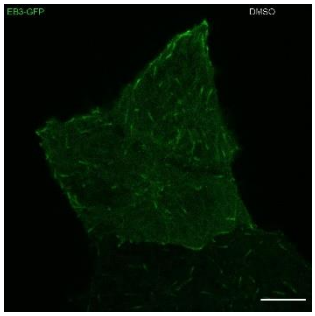

Movie 11. Rat2 cells that were electroporated with a plasmid that encoded EB3-GFP and treated with 0.1% DMSO for 1 h. Speed = 10x real time. Scale bar = 10 μm.

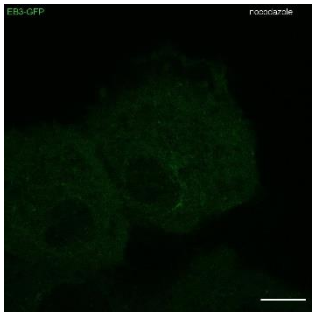

Movie 12. Rat2 cells that were electroporated with a plasmid that encoded EB3-GFP and

treated with 100 nM nocodazole for 1 h. Speed = 10x real time. Scale bar = 10 μm.

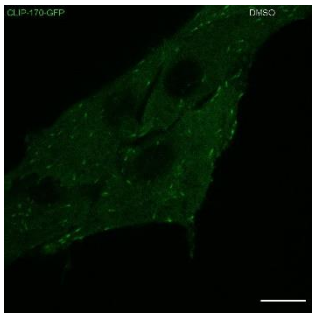

Movie 13. Rat2 cells that were electroporated with a plasmid that encoded CLIP-170-GFP and treated with 0.1% DMSO for 1 h. Speed = 10x real time. Scale bar = 10 μm.

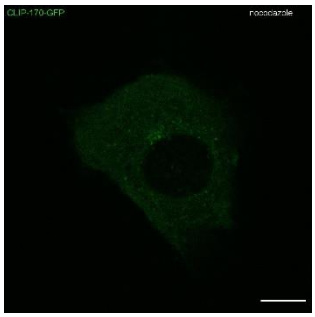

Movie 14. Rat2 cells that were electroporated with a plasmid that encoded CLIP-170-GFP and treated with 100 nM nocodazole for 1 h. Speed = 10x real time. Scale bar = 10 μm.

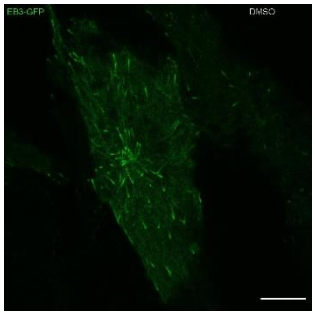

Movie 15. Rat2 cells that were electroporated with a plasmid that encoded EB3-GFP and treated with 0.1% DMSO for 2 h. Speed = 10x real time. Scale bar = 10 μm.

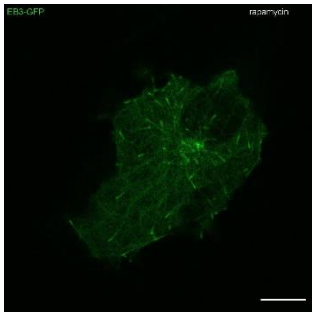

Movie 16. Rat2 cells that were electroporated with a plasmid that encoded EB3-GFP and treated with 100 nM rapamycin for 2 h. Speed = 10x real time. Scale bar = 10 μm.

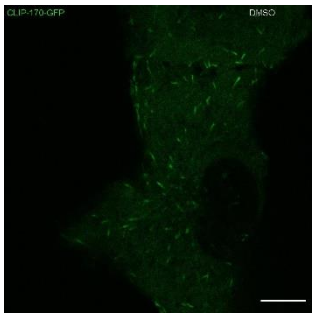

Movie 17. Rat2 cells that were electroporated with a plasmid that encoded CLIP-170-GFP and treated with 0.1% DMSO for 2 h. Speed = 10x real time. Scale bar = 10 μm.

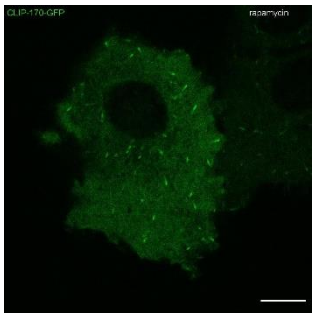

Movie 18. Rat2 cells that were electroporated with a plasmid that encoded CLIP-170-GFP and treated with 100 nM rapamycin for 2 h. Speed = 10x real time. Scale bar = 10 μm.